9th IAA Planetary Defense Conference – PDC 2025
5–9 May 2025, Stellenbosch, Cape Town, South Africa

IAA-PDC25-06-231

Pulverize It (PI): Intentional Robust Disruption for Multi-modal Planetary Defense

Brin Bailey[a,1,*], Alexander N. Cohen[a,2], Sasha Egan[b,3], Philip Lubin[a,4], Ruitao Xu[a,1], Mark Boslough[c,5], Peter Meinhold[a,6], Scott Taylor[a,6]

[a] *University of California, Santa Barbara, Santa Barbara, California 93106, USA*
[b] *New Mexico Institute of Mining and Technology, EMRTC, 801 Leroy Place, Socorro, New Mexico 87801, USA*
[c] *University of New Mexico, 1700 Lomas Blvd, NE. Suite 2200, Albuquerque, New Mexico 87131, USA*

Abstract

Pulverize It (PI) is a planetary defense concept which is designed to operate in both short-warning and extended time scale interdiction modes, representing a unique multi-modal approach to asteroid threat mitigation. PI is under development as part of a NASA Innovative Advanced Concepts (NIAC) Phase II study. The method utilizes high-density hypervelocity impactors to penetrate and fragment an incoming asteroid. In extended warning scenarios in which the asteroid is intercepted far from Earth, PI can be used for either robust disruption via complete fragmentation or enhanced deflection via partial fragmentation. In short-warning scenarios, PI can be used in a terminal mode to disrupt an incoming asteroid into small fragments ($<$10 m diameter) which then intercept Earth, resulting in a series of high-altitude airburst events with spatial and temporal spread. This yields ground-level optical pulses and de-correlated shock waves which distribute the energy of the parent asteroid.

PI represents the first planetary defense method with multi-modal capability and with the ability to respond to rapid, short-warning threats. We analyze the effectiveness of mitigation via intentional robust disruption (IRD) for objects similar to 2024 PDC25, the 90-160 m diameter threat described in the 2025 Planetary Defense Conference (PDC) Hypothetical Asteroid Impact Scenario. We compare PI to kinetic impact (deflection) by simulating mitigation of a Dimorphos-scale (160 m diameter) asteroid model to compare with NASA's Double Asteroid Redirection Test (DART) mission. We find that, in general, PI requires a lower launch mass than kinetic impact missions for the same threat, which enables a fully capable planetary defense system that relies solely on pre-existing launch vehicles. Our simulations support the proposition that PI is an effective multi-modal approach for planetary defense, particularly for objects within the diameter range of 2024 PDC25, even in terminal interdiction modes which yield ground effects that are vastly less damaging in comparison to unmitigated cases.

Keywords: Planetary defense, hypervelocity impacts, disruption, fragmentation

---

1. Introduction

1.1. 2025 Planetary Defense Conference Hypothetical Asteroid Impact Scenario

In a scenario in which a large asteroid is on a collision course with Earth, threatening an impact with potential regional devastation in under 20 years, there is little room for error. This is the case with

---

[*] Corresponding author
Email address: `brittanybailey@ucsb.edu` (Brin Bailey)
[1] Assistant Specialist, Department of Physics
[2] Research Specialist, Department of Physics
[3] Research Engineer, Energetic Materials Research and Testing Center
[4] Director, UCSB Experimental Cosmology Laboratory
[5] Research Professor, Department of Earth and Planetary Sciences
[6] Research Physicist, Department of Physics

the 9th International Academy of Astronautics (IAA) 2025 Planetary Defense Conference's hypothetical asteroid impact scenario, a biannual emergency response exercise with international collaboration.

For each meeting, a simulated asteroid threat scenario is designed. Realistic astronomical data and analyses of the "asteroid" are released over the span of several months leading up to the meeting, emulating a real-world incident. This exercise is entirely fictional and is meant to prepare researchers, institutions, and organizations for a potential future real-life threat scenario. All asteroid parameters discussed throughout this paper are fictional unless designated otherwise.

1.1.1. Epoch 1: August 2024

The 9th IAA Planetary Defense Conference (PDC) focuses on a hypothetical, mid-to-large-sized asteroid designated as *2024 PDC25,* discovered about 17 years before a potential impact [1]. When first detected on 5 June 2024, the object is distanced about 0.233 au from Earth, making the asteroid's physical and orbital characteristics difficult to constrain. Initial orbital assessment finds that the object is on an orbit that could approach very close to Earth's orbit, well within 0.05 au.

On 1 August 2024, approximately two months after the discovery of 2024 PDC25, space-based infrared observations yield an estimated size range of 48 – 278 m in diameter, though most likely between 89 – 155 m, with a median of 125 m [1]. These observations also find that the asteroid belongs to the S-type taxonomic class, with bulk density ranging from $\sim$1.1 – 2.8 g/cm^3, most likely $\sim$1.6 – 2.7 g/cm^3, and macroporosity between 0 – 60%. Due to the combination of the asteroid's preliminary size estimate and the closeness of its orbit with Earth's, 2024 PDC25 is categorized as a Potentially Hazardous Asteroid (PHA).

It is found that 2024 PDC25 will make a close approach to Earth in April 2041, with an impact probability initially estimated at 1.6% [1]. If impact occurs, it is expected to release energy equivalent to 5 – 70 Mt, but possibly in the range of 3 – 720 Mt, yielding regional blast damage extending $\sim$40 – 200 km from the impact location.

1.1.2. Epoch 2: April 2028

On 29 September 2025, it is found that 2024 PDC25 will impact Earth with 100% certainty on 24 April, 2041 [2]. In September 2027, a fast flyby reconnaissance mission is launched to encounter the asteroid in April 2028, aiming to directly measure the asteroid's size and composition. Observations reveal an elongated asteroid with an approximate 2:1 aspect ratio and constrain its size as between 145 – 155 m (spherical equivalent). The asteroid is confirmed as an S-type, implying a stony composition, with density likely still between $\sim$1.6 – 2.7 g/cm^3. However, its structure, strength, and breakup properties remain uncertain, with possibilities ranging from a weak rubble pile to a strong monolithic body.

Combining the asteroid's estimated physical properties with its expected impact velocity of 13.725 km/s yields impact energies ranging from $\sim$45 – 160 Mt, though most likely between $\sim$60 – 105 Mt [2]. It is expected to impact with an entry angle of $\sim$69° with a northward heading.

A combination of continued ground observations and data collected by the flyby mission greatly reduce the uncertainty in the object's orbit, resulting in a very narrow impact risk corridor spanning Angola and the Democratic Republic of the Congo. The damage is expected to be regional, most likely affecting hundreds of thousands of people, with a potential range between tens of thousands to over a million depending on impact location and damage areas.

The primary hazard is a large, destructive blast wave from a high-energy, low-altitude airburst. Ground damage near the blast would likely reach unsurvivable levels, with serious damage likely extending out to $\sim$100 – 120 km or possibly further. While less severe than the blast damage, thermal damage from larger fireballs could extend out to $\sim$0 – 14 km or possibly as far as 40 km in radius [2].

1.2. Near-Earth Asteroid Risks

While 2024 PDC25 is a hypothetical scenario, it is conceivable that a similar threat could arise in the future. While detection rates for very large threats ($>$1 km) are reasonably fulfilled, our situational awareness for smaller asteroids ($<$140 m diameter), which constitute the most common threats in the solar system, is poor. As of April 2025, it is estimated that about 95% of near-Earth asteroids (NEAs) $>$1 km in diameter have been discovered, for which there is an estimated population between 920 — 940 [3, 4]. In comparison, estimates suggest that approximately 45% of NEAs $>$140 m have been discovered, for which there is an estimated population of about 25,000 [3]. For NEAs $<$140 m, a 2021 study by Harris and Chodas estimate a population of approximately 2.88×10^9, though this value has a large degree of uncertainty [4]. As asteroid diameter decreases, the likely population increases drastically, thus decreasing our estimated discovery ratio.

Given the power law of threat incidence versus diameter and a lower threshold of approximately 20 m in diameter for what are considered "significant" threats (for rocky compositions), our situational awareness is severely limited in the smaller threat regime. This issue may have two solutions, distinct in approach but aligned in goal: 1) enhancing small-threat situational awareness through heightened detection efforts, and 2) augmenting these efforts by establishing effective short-term mitigation systems. Both strategies could theoretically be enhanced concurrently to accelerate the development of a robust planetary defense program.

1.3. Motivation for Short-term Mitigation

In an idealized mitigation scenario, one would strive for threat interception to occur as far away–in both space and time–from Earth as possible. However, reality may make such a desirable outcome improbable to impossible, due to hurdles like uncertainty in the threat's characteristics or lack of time for preparation. In a scenario where extended warning time and preparation are out of reach, it is imperative to consider terminal mitigation methods.

In situations with warning times on the scale of months to a few years, deflection-based mitigation strategies may fall short of preventing damage. The time taken to plan, assemble, launch, and successfully deflect with enough momentum transfer is likely to be on the scale of years, if not decades. To achieve an extensive planetary defense system, preparedness for a variety of threat scenarios–considering a large range of threat sizes and warning times–is imperative. It can be argued that such a system would not be limited to a single strategy, but would instead be comprised of a layered structure of reliable, tested methods for both detection and mitigation to achieve such preparedness.

There is currently no planetary defense solution in place that allows for short-warning mitigation. In the case of a short-warning threat scenario, it may be desirable to consider a mitigation method with the capability for rapid deployment using preexisting technologies. We present Pulverize It, a multi-modal mitigation method that provides at-the-ready capability with the potential for a single-launcher solution [5, 6, 7].

2. Pulverize It for Planetary Defense

2.1. Introduction to Pulverize It

Pulverize It (PI) is a NASA Innovative Advanced Concepts (NIAC) Phase II study of planetary defense which is intended to operate in both short-warning and extended interdiction modes, representing a fundamentally different approach to threat mitigation. Planetary defense has traditionally focused on mitigation via orbital modification, or deflection, utilizing momentum transfer to prevent an impact. Mitigation via deflection has explored a wide range of possible techniques, ranging from impulsive methods, like direct impact or nuclear ablation [8, 9], to gradual orbit deflection (e.g., via surface albedo alteration) [10], to the utilization of gravity tractors, ion engines, laser ablation, and other developing technologies [11, 12]. Alternatively, PI uses energy transfer for mitigation, aiming to fragment a threat via intentional robust disruption (IRD) rather than deflect it. The method utilizes an array of hypervelocity kinetic penetrators that disassemble an asteroid into many small (typically $<$10 m) fragments [5].

Depending on the time scale of interception, the fragment cloud either misses Earth entirely (long-warning time) or is dissipated in Earth's atmosphere (short-warning time, henceforth referred to as the "terminal mode") [5]. The latter results in a series of airburst events with spatial and temporal spread at varying high altitudes, which distributes the energy of the parent asteroid [5, 13].

2.2. Extended Interdiction Mode

PI's preferred mode of operation is its extended interdiction (long-warning) mode, where a threat is intercepted months or years ahead of Earth impact (with idealized intercept times depending largely on threat size and velocity, among other parameters). In such a case, the resulting fragment cloud spreads far enough to miss Earth entirely, completely removing the threat.

PI can be used in a variety of modes catered to the specific threat. In a standard fragmentation operation, an array of kinetic (passive) penetrators can intercept the asteroid, with desired cumulative intercept mass depending largely on the size, velocity, structure, and yield strength of the threat. A configuration of sequential penetrators, spaced apart by an idealized distance, can create a "hole-drilling" effect in which following penetrators will enter deeper into the target, allowing for improved fracture and disruption [5, 6].

In scenarios with very large and/or high-strength threats, the standard fragmentation mode could optionally be enhanced by use of conventional explosives or a nuclear explosive device (NED). An explosive package could be safely delivered into the body of the asteroid following a series of sequential penetrators, allowing for enhanced energy coupling. A full investigation of IRD via NEDs is outside the scope of this paper; more thorough discussions can be found in Lubin and Cohen [5] and an additional forthcoming study.

Additionally, in scenarios with warning times on the scale of years or decades, the standard fragmentation mode could be adapted into an enhanced momentum transfer option, wherein partial or asymmetrical fragmentation of a threat could eject a significant fraction of the target mass to induce large momentum transfer. This could be achieved via use of only kinetic penetrators, kinetic with conventional explosives, or kinetic with NED delivery for extreme threats. A more thorough discussion of PI in its extended warning and enhanced deflection modes can be found in Lubin and Cohen [5, 6].

2.3. Terminal Interdiction Mode

We intend for the use of PI in its terminal mode to be reserved for extreme cases where there is little to no time before impact, in which there would be no other mitigation option. When feasible, it is preferable to keep any planetary defense operation as far from Earth as possible to mitigate any potential damage on the ground. However, it is reasonable to imagine a case in which early warning is not provided or opportunities for early mitigation are lacking. In a hypothetical "worst-case" scenario, PI could be deployed terminally as the first planetary defense option for short-warning threats.

As such, note that the methodology described within this section, as well as the simulated terminal scenarios presented in Section 4, focus only on such "worst-case" scenarios in which longer-timescale mitigation would be unfeasible. Even in the hypothetical case of 2024 PDC25–whether assuming implementation of PI as fully established or not yet realized–it would be highly unlikely that deployment of PI would be held off long enough that a terminal mitigation scenario would occur. This consideration is explored further within Section 5.

Mitigation of a threat by using PI in a terminal mode consists of two stages: 1) interception and fragmentation of the asteroid and 2) dissipation of the fragment cloud within Earth's atmosphere. In such cases, the primary mechanism for threat mitigation is the distribution of the asteroid's energy into the fragment cloud, resulting in spatially and temporally de-correlated ground effects.

In the terminal mode, the impacting fragment cloud interacts with Earth's atmosphere in a manner similar to an unmitigated asteroid airburst, but instead disperses the energy relative to the unmitigated case [5]. During atmospheric entry of the fragments, the high-velocity ram pressure (or stagnation pressure) exerted by the atmosphere eventually exceeds the material yield strength, initiating a cascading breakup event [14, 15]. The ram pressure is determined by the density of the atmosphere and velocity of the parent asteroid, whereas yield strength depends largely on the shear strength provided by the internal structure and integrity of the asteroid, including the strength of its components (as well as other parameters such as size, density, velocity, and entry angle) [15]. As the pressure buildup on the fragment increases, it undergoes ablation and begins to flatten and expand, increasing the surface area on which the rising aerodynamic drag can act [14]. This runaway process eventually converts the fragment's kinetic energy into a release of heat and pressure through detonation, or "bursting," of the fragment [14].

Depending on the material strength, initial failure can occur either externally or internally; the failure site will influence the method by which the fragment bursts [15]. These airbursts yield optical pulses and de-correlated shock waves on the ground (hereafter referred to as "ground effects") which, in reasonable mitigation scenarios that are appropriate for the threat, result in little to no damage.

3. Hypervelocity Interception and Fragmentation

3.1. Material Models

We simulate hypervelocity impacts with the Lawrence Livermore National Laboratory (LLNL) arbitrary Lagrangian-Eulerian (ALE) hydrodynamics code ALE3D [16]. We run ALE3D on the High-End Computing Capability (HECC) at NASA Ames Research Center. Using ALE3D, we model hypervelocity impact dynamics in 2D and 3D using equation-of-state material models which include shock response, material vaporization/ionization, and porous crush. We make use of the Livermore Equation of State (LEOS) tables as the building blocks of our material models. The simulation results are used to better understand how disruption capability changes as the target size increases, and to better understand the

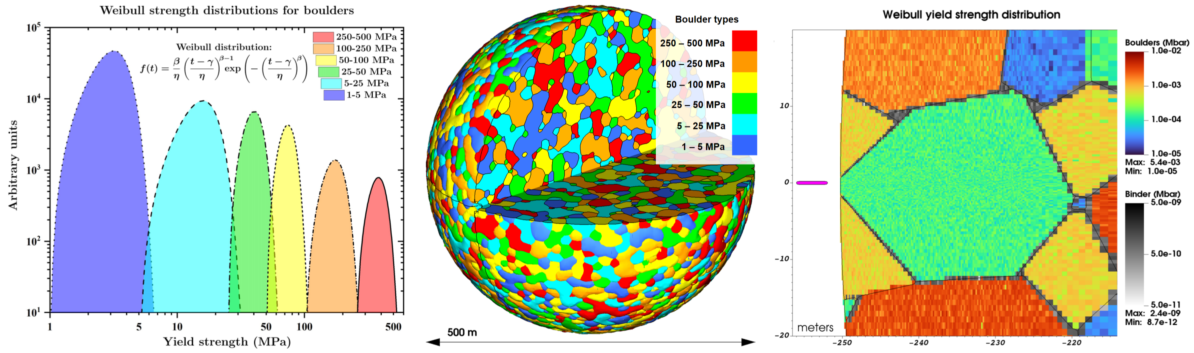

Figure 1: Our asteroid models contain boulders of six different types, each with unique internal strengths which vary in ranges specified by the Weibull distributions at left above. In addition, there is a weak binder material with its own Weibull strength distribution (average 25 Pa yield strength) which fills the volume between boulders, as shown at right above. The middle figure shows the rubble pile asteroid model in partial cross section for a 500 m diameter bolide. The boulder distribution within is colored by the material yield strength ranges, corresponding to the distributions at the left above. On the right above is a cross sectional view of the region local to the penetrator impact site. The color plot shows the different Weibull strength distributions of the boulders in Mbar (1 Mbar = 10^5 MPa, penetrator shown in magenta), and the greyscale plot shows the Weibull strength distribution in the binder material.

effect of asteroid material properties on the dynamics of hypervelocity impact events and total disruption of the target.

Our baseline bolide model consists of a sphere of weak binder material (25 Pa average yield strength) and a distribution of boulders of varying strength embedded within it. Each boulder is assigned to one of six boulder types, each with a different Weibull strength distribution, ranging from 1 – 5 MPa to 250 – 500 MPa, as shown in Figure 1. The binder material also has a Weibull strength distribution with an average value of 25 Pa, also shown at the right in Figure 1. Note that the boulder strengths used here are a conservative over-estimation of the strength of rubble pile asteroids [17, 18]. Unlike our earlier simulations which used spherical boulders [5], the boulders here are of a granular nature with up to 30 facets. We use LEOS table 4030 for granite with density 2.67 g/cm^3 as our baseline material model for both the boulder distribution and the weak binder material, and we model the effect of porosity in the presence of shocks with a porous crush model. As per work done by Housen et al. [19], we specify initial porous crush pressures of 100 MPa and ~ 30 MPa for the boulder and binder material respectively, which corresponds to 40% porosity in the boulder material and 50% porosity in the binder material. Both the boulder and binder materials make use of a damage model which modulates the yield strength via the material damage parameter $0 \leq D \leq 1$, where $D = 1$ corresponds to completely failed material. Failure refers to when the material can no longer support tensile stresses, but still retains compressive strength.

Our passive penetrators are modeled as 10:1 aspect ratio tungsten cylinders. We use LEOS table 740 for tungsten with density 19.24 g/cm^3 as our penetrator material model in addition to a bilinear yield curve model with 750 MPa yield stress. While our earlier simulations made use of 100 and 500 kg penetrators, for this work we extend the penetrator mass to 2.5, 10, and 100 metric tons to aid in the disruption or deflection of targets in the 100 – 1000 m diameter range. These penetrator masses also correspond to the estimated maximum payload capacities of the SpaceX Falcon 9, Falcon Heavy, and Starship, respectively.

3.2. Simulation Parameters

We conduct our hypervelocity impact simulations in two phases: an initial phase with high spatial and temporal resolution which fully resolves the penetrator radius and portion of the asteroid volume local to the impact site, followed by a lower resolution phase with a much larger simulated region and a much longer time scale. The early time simulations typically run with a time step of 1 – 10 microseconds out to approximately 10 milliseconds after impact, and with a spatial resolution of 10 cm^3 local to the impact site (this resolution is greatly reduced as the distance from the impact site increase). The later time simulations run from 10 milliseconds out to macroscopic time scales on the order of tens of seconds or minutes after impact, with time steps of 0.1 – 1 millisecond and spatial resolution of 1 – 25 m^3. The time step magnitude in both the early and late time simulations is generally driven by the sound crossing speed of the smallest cell in the simulation, and thus is much smaller in the early time simulations where the spatial resolution is higher. The minimum spatial resolution is driven by the minimum acceptable fragment size we wish to resolve, which is generally limited to 10 m in diameter [5, 7, 13].

In order to extend our late time simulations out to macroscopic timescales while optimizing for computational cost, we implement a density threshold of 10^{-3} g/cm^3 below which material is removed from the calculation. This density threshold is not enforced during the early time simulations, where low density, high temperature and pressure material trapped within the impactor entrance cavity is still an important factor in the disruptive capability of the impact event. However, after transitioning to the late time simulations, the disruption dynamics become predominantly inertial and the low density material is no longer contributing to the expansion of the entrance cavity, and is thus regularly removed from the calculation to reduce computational complexity.

3.3. Robust Disruption of 20 – 100 m Diameter Targets

Figure 3 shows a plot of material density before and after a simulated hypervelocity impact event which achieves catastrophic disruption of a 100 m diameter rubble pile asteroid target. This simulation uses the 2.5 metric ton, $C_3 > 0$ payload capacity of a SpaceX Falcon 9 as discussed above as the penetrator mass, in the usual form of a 10:1 aspect ratio tungsten cylinder with a closing speed of 20 km/s. The total mass of the original bolide is $M_{100m} \approx 5.143 \times 10^8$ kg, which results in a gravitational escape speed of $v_{esc} \approx 0.037$ m/s at the surface. At $t = 11$ seconds after impact, the average fragment speed is ~ 10.6 m/s and the bowl-shaped remnant shown at the right of Figure 3 continues to dissociate into fragments with an average radial speed of 2.5 m/s, which is greater than $60\times$ the gravitational escape speed. At this time, the remaining material has an average material damage parameter of $\langle D \rangle = 0.937$.

3.4. Enhanced Deflection of a 500 m Diameter Target

A partial cross section view of our 500 m diameter rubble pile asteroid model is shown at the center in Figure 1. As described in above, it is comprised of a granular boulder distribution set within a sphere of weak binder material. The total mass of the bolide is $M_{500m} \approx 6.723 \times 10^{10}$ kg, or about 67 million metric tons, which results in a gravitational escape speed of $v_{esc} \approx 0.189$ m/s at the surface. Our baseline mitigation scenario for this case is a 20 km/s impact with a 10 metric ton, 10:1 aspect ratio tungsten cylinder (after meshing, the penetrator mass is measured to be $M_{500m} \approx 1.014 \times 10^4$ kg).

The sequence of frames in Figure 2 shows the time evolution from 100 milliseconds to 1 minute after impact for the above baseline mitigation scenario of our 500 m diameter asteroid model shown in Figure 1. Fragment statistics in the form of fragment mass, diameter, and speed distributions are plotted in Figure 4 at $t = 60$ seconds after impact. At this time in the simulation, we resolve 751 fragments at 25 m^3 mesh resolution, with an average mass, speed, and size of 10^6 kg, 5.9 m/s, and 9.2 m in diameter. The maximum fragment mass, speed, and size is 1.5×10^7 kg, 11.3 m/s, and 27.2 m in diameter (note that these values do not correspond to the same fragments). From the fragment speed distribution in Figure 4 (red histogram) it can be seen how all of the fragments have speeds above the gravitational escape speed of 18.9 cm/s of the parent bolide, and the average fragment speed of 5.9 m/s is $> 30\times$ the gravitational escape speed. From the fragment masses and speeds, we can calculate the fraction of penetrator kinetic energy which has been transferred to the fragments. Of the roughly 2 TJ of kinetic energy delivered by the 10 metric ton penetrator with closing speed 20 km/s, approximately 0.67%, or ~ 13.6 GJ, has been converted into fragment kinetic energy in the target's original rest frame.

The three inset color plots in Figure 2 show the material damage parameter $0 \leq D \leq 1$ along 2D equatorial cross sections of the bolide at $t = 100$ milliseconds, 1 second, and 10 seconds after impact. At $t = 10$ seconds the damage parameter takes an average value of $\langle D \rangle = 0.714$.

As per the work done by Housen and Holsapple in [20, 21, 22], we define the momentum enhancement factor in an asteroid deflection scenario as

$$\beta = M\,\Delta V\,/mv, \tag{1}$$

where M is the target bolide mass, ΔV is the change in speed of the target bolide, m is the penetrator mass, and v is the penetrator closing speed. At 60 seconds after impact, we measure $\Delta V_{500m} \approx 0.246$ m/s, which allows us to calculate that the momentum enhancement factor achieved is $\beta_{500m} \approx 81.6$. This is an extremely high β value. For reference, the estimated β value for the DART mission is ~ 3.61,

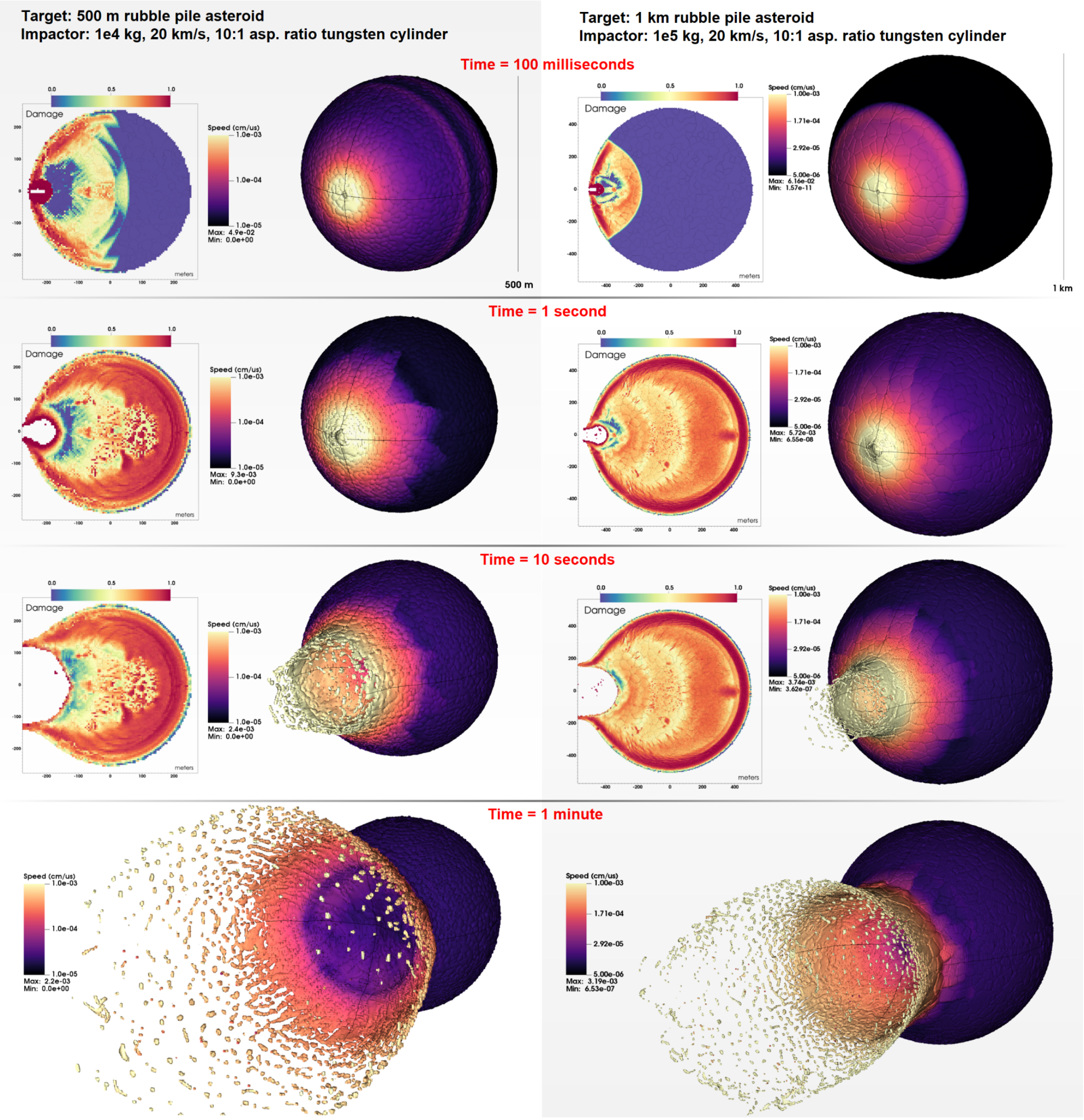

Figure 2: (left) Time evolution of a 20 km/s impact of a 10 metric ton, 10:1 aspect ratio tungsten penetrator upon a 500 m diameter rubble pile asteroid. The 3D plots show the material speed in centimeters per microsecond at 0.1, 1, 10, and 60 seconds after impact. At 60 seconds after impact, we calculate that the momentum enhancement factor achieved is $\beta_{500\text{m}} \approx 81.6$. Inset 2D figures: material damage parameter $0 \leq D \leq 1$. After 1 second, the material damage distribution remains mostly static. (right) Time evolution of the same penetrator incident upon a 1 kilometer diameter rubble pile asteroid. At 60 seconds, we calculate that the momentum enhancement factor achieved is $\beta_{1\text{km}} \approx 41.3$.

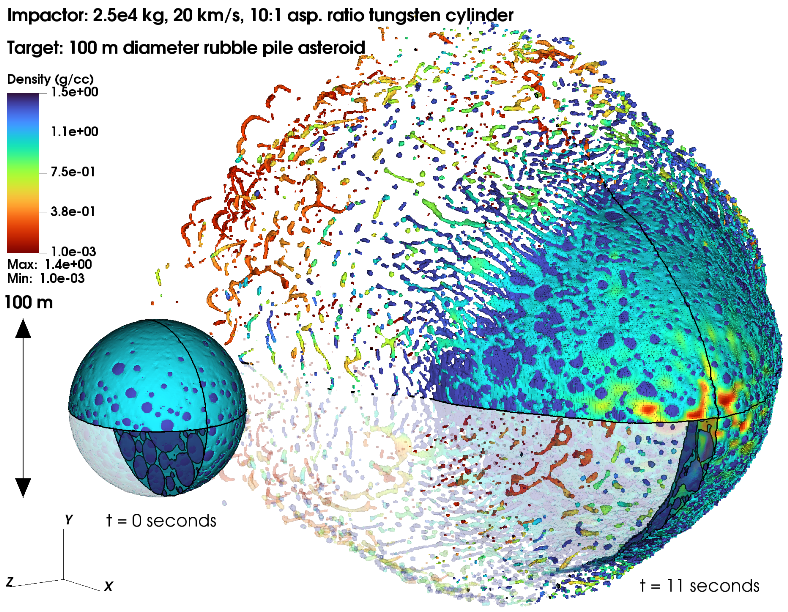

Figure 3: Robust disruption of a 100 m diameter asteroid via the 20 km/s impact of a 2.5 metric ton, 10:1 aspect ratio tungsten cylinder penetrator. The bolide prior to impact is shown on the left, and the aftermath of the impact at 11 seconds is shown on the right. The color plot shows the material density in grams per cubic centimeter.

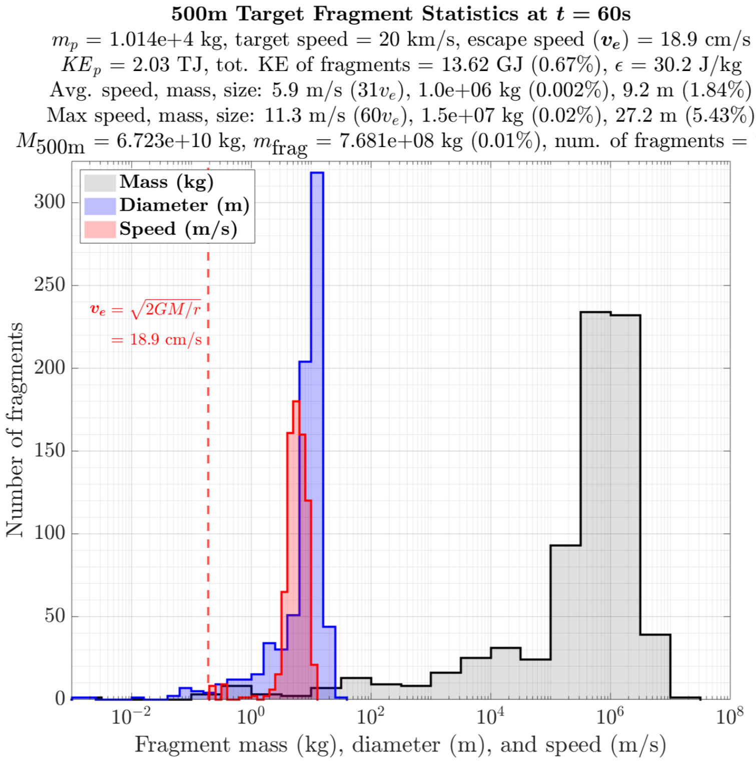

Figure 4: Fragment statistics at 60 seconds after 20 km/s of a 10 metric ton, 10:1 aspect ratio tungsten penetrator upon a 500 m diameter rubble pile asteroid. Fragment masses, diameters, and speeds are shown as black, blue, and red histograms, and the gravitational escape speed is shown as a dashed red vertical line. Average and maximum fragment properties are listed in the title. Note how the average fragment speed is $> 30\times$ the gravitational escape speed. At this time, we measure a specific impact energy of 30.2 J/kg, and approximately 0.67% of the penetrator kinetic energy has been transferred to the fragments. The total mass in fragments is 0.01% the original target mass.

which delivered ~ 570 kg of spacecraft mass to impact the asteroid Dimorphos at ~ 6.6 km/s [23]. A more accurate value of β for our simulations would take into account the low density material which is removed from our calculations in the late time phase since much of this low density material travels at high velocities roughly in the direction opposite penetrator. However, it amounts to only a small fraction of the total mass (of order 0.01% or less) and does not significantly contribute to the total momentum imparted to the target [21]. This extremely high β result motivates the enhanced and classical deflection modes of operation with extended warning times > 1 year.

3.5. *Enhanced Deflection of a 1 km Diameter Target*

The total mass of our 1 km asteroid model is $M_{1km} \approx 6.267 \times 10^{11}$ kg, or about 627 million metric tons, which results in a gravitational escape speed of $v_{esc} \approx 0.409$ m/s at the surface. Our baseline mitigation scenario for this case is a 20 km/s impact with a 100 metric ton, 10:1 aspect ratio tungsten cylinder (after meshing, the penetrator mass is measured to be $m_{1km} \approx 9.794 \times 10^4$ kg). The sequence of frames in Figure 2 shows the time evolution from 100 milliseconds to 1 minute after impact for the above baseline mitigation scenario.

The three inset plots in Figure 2 show 2D equatorial cross sections of the bolide at $t = 100$ milliseconds, 1 second, and 10 seconds after impact. The color plot shows the material damage parameter $0 \leq D \leq 1$, and at $t = 10$ seconds the damage parameter takes an average value of $\langle D \rangle = 0.734$.

As was done for the 500 m diameter case above, at 60 seconds after impact we measure $\Delta V_{1km} \approx 0.129$ m/s, which allows us to calculate that the momentum enhancement factor achieved is $\beta_{1km} \approx 41.3$. This result motivates the enhanced and classical deflection modes of operation with extended warning times > 1 year, and the long warning mitigation of existential threats in the 1 – 15 km diameter range.

4. Ground Effects

Following interception and disassembly of the asteroid in a terminal mitigation scenario, its initial exo-atmospheric kinetic energy is distributed into the fragment cloud, which, upon entry with Earth's atmosphere, results in a series of airburst events. We simulate the ground effects produced by these airburst events for the terminal mode relevant in this paper via computation of the optical pulse model and analytic airburst model for a given scenario.

A full description of the methodology and simulation process for the ground effects models–including parameter definition, computation, and statistical variation–can be found in [13].

4.1. *Optical pulse modeling*

The conversion of kinetic energy into optical energy is highly dependent on fragment properties, particularly cohesive strength, and is poorly understood in general. We resort to measured optical data to model this conversion, primarily from Department of Defense satellite observations of a small number of relevant bolide sizes of interest to us (typically 1–15 m in diameter) [24]. Using an analytical extrapolation from [24], we calculate the optical energy flux at burst (in Joules) from exo-atmospheric energy E_{exo} as

$$E_{opt} = \left(\frac{E_{exo}}{8.2508}\right)^{1.13}. \tag{2}$$

For the propagation of the optical pulse through the atmosphere, we use a full radiation transfer model to compute the optical power flux from each fragment at each observer. Because the optical propagation is occurring at very close to the speed of light in vacuum and the relevant distance scales from the fragment to the observer are of order of tens to hundreds of km, the light propagation time scale is very short. The optical pulse can then be well approximated as happening nearly simultaneously at all observer points, with the optical pulse arriving very shortly after the fragment burst.

As a result, we propagate the optical energy flux to each observer using the distance propagation of light, inputting E_{opt} at the time of burst to simulate an instantaneous addition of energy flux [5, 13]. We propagate the optical emission from every fragment to the observer to get a total energy flux at the observer.

4.1.1. Atmospheric attenuation and cooling

Several factors can greatly affect the observed optical flux, such as the source spectral energy distribution and atmospheric attenuation, which depend on both the source and the complex and time-varying nature of the atmosphere [25]. To calculate the attenuation of the optical signature, we approximate the parent asteroid as a blackbody source due to the wavelength-dependent transmission of the atmosphere. We model the atmosphere using MODTRAN to perform a full analysis of attenuation which includes the curvature of Earth's atmosphere and the relationships between nominal atmospheric pressure, temperature, and altitude [5].

Note that we assume an extremely conservative case of no cooling at the observer between fragment optical pulses. However, in a real scenario, fragments arrive on the order of tens of seconds apart (to hundreds of seconds in some extreme cases), which would, in general, be enough time for significant cooling between bursts of incident optical energy. This will be important when judging the effectiveness of this method if the energy exceeds our threshold.

4.2. Acoustic shock wave modeling

The acoustic ground effects from an asteroid fragment airburst can be related to and approximated by those of nuclear blasts, as discussed by Boslough et al [26]. We then base our simulations of the acoustic ground effects from mitigation via PI on measurements of equivalent nuclear blasts. To model the time evolution of the shock wave, we use a Friedlander functional form, given by

$$p(t,r) = p_0(r)e^{-t/t_1}(1 - t/t_1), \tag{3}$$

which describes the shock wave time evolution at a distance r with two free parameters: the peak pressure p_0 in Pa at time $t = 0$ seconds and the Friedlander positive pulse time scale, or zero crossing time, t_1 in seconds [13]. Note that the time $t = 0$ seconds is the time at which the shock wave first arrives at the observer, not to be confused with the time at which the fragment bursts.

Letting ϵ denote the fraction of a 1 kt yield that goes into the shock wave (typically 0.5), we achieve $E_{nuc} = E_{ast-kt}/\epsilon$, where E_{ast-kt} is the asteroid airburst shock wave energy and E_{nuc} is the equivalent energy of a nuclear weapon [5]. The peak pressure at a distance r is calculated from the equivalent energy of a nuclear weapon as

$$p(r) = p_n[rE_{nuc}^{1/3}]^{\alpha_n} + p_f[rE_{nuc}^{1/3}]^{\alpha_f}, \tag{4}$$

where $p_n = 3.11 \times 10^{11}$ Pa is the pressure for a 1 kt standard weapon yield in the near field, $\alpha_n = -2.95$ is the power law index for the near field, $p_f = 1.80 \times 10^7$ Pa is the pressure for a 1 kt standard weapon yield in the far field, and $\alpha_f = -1.13$ is the power law index for the far field [5].

We simulate the airburst produced by each fragment as it enters Earth's atmosphere using equations (3) and (4). The model considers any interference between interacting shock waves, summing them to simulate the acoustic caustics.

4.3. Damage Thresholds

The ground effects of unmitigated asteroids or large fragments (>20 m) have the potential for significant destruction; we therefore design mitigation scenarios such that the fragments are generally <10 m in diameter [5]. It is important to analyze both the optical and acoustic ground effects to design proper mitigation scenarios with acceptably low damage.

Total energy deposition from thermal radiation can result lead to effects such as fires, skin burns, and eye injuries to exposed persons [25]. We set an optical energy damage threshold of 200 kJ/m^2 so that the sum of the optical energy taken over all fragments (assuming the analytic relationship outlined in Section 4.1) is kept below this value. We chose a value of 200 kJ/m^2 (~5 cal/cm^2 of radiant exposure), as this is the point at which combustible organic materials (like leaves and paper) can begin to catch fire [27].

For acoustic effects, studies of window damage in atmospheric nuclear tests [25] have found that the threshold for residential window breakage corresponds to peak pressures of about 3 kPa. PI therefore sets a shock wave over-pressure threshold of 3 kPa, with the goal in any mitigation scenario being to keep all shock wave over-pressures (including constructive interference) below this value.

4.4. Simulation Parameters

As is discussed later in Section 5, it would be extremely conservative to assume that the hypothetical impact scenario for 2024 PDC25 would necessitate a terminal mitigation effort. With discovery and flyby of the asteroid taking place roughly 17 years and 13 years prior to impact respectively, it would be reasonable to assume that a mitigation mission could be launched years ahead of the April 2041 impact date. However, as part of a full investigation into both the hypothetical impact exercise and the multi-modal utilization of PI, we simulate here the ground effects from various terminal mitigation efforts of 2024 PDC25. Note that these cases should be interpreted as worst-case scenarios in which other options are unavailable, or as "backup" operations in the event an initial mission fails or results in unintended or unsuccessful disruption.

4.4.1. Physical and Entry Characteristics of 2024 PDC25

As the property statistics of 2024 PDC25 are computed independently and cannot necessarily be combined to represent a single physically plausible asteroid, our ground effects simulations span the diameter and density ranges estimated throughout Epochs 1 and 2 [28, 29]. For each diameter estimate from 50 – 280 m (spherical equivalent), there are fourteen different models of average density ranging from 1.0 – 4.0 g/cm^3 (Table 1). Impact energies range from ~1.5 – 1000 Mt.

For the diameter range of 50 – 90 m, we additionally simulate and compare the ground effects from equivalent unmitigated asteroid airbursts. Each diameter estimate is computed with four separate density models, with average densities spanning the "most likely" (68th %) range of 1.6 – 2.8 g/cm^3 (Table 2).

Each of the ground effects simulations assumes an entry angle of 69° from horizontal and entry velocity of 13.725 km/s. While these parameters are specific to impact entry and are not necessarily directly relatable to the orbital angle and velocity at the time of a potential intercept, we use them as a baseline for the terminal scenarios presented here, so as to somewhat standardize parameters between different cases.

4.4.2. Mitigation Scenario Characteristics

As is discussed in Section 5.2, intercept time is a critical component in the outcome of a mitigation effort. If one is to conservatively assume that development of PI would be delayed, or perhaps that a secondary mission is necessary following unsuccessful deflection or disruption initially, a terminal mitigation effort could remain feasible. Most of the ground effects simulations assume an extreme intercept time of 30 days prior to Earth impact, which (depending largely on target and spacecraft velocities) would require a launch on the scale of ~60 – 150 days before impact. Particular attention is paid to the most likely diameter and density ranges of 140 – 160 m and 1.6 – 2.8 g/cm^3, for which we additionally simulate intercept times of 180 days (cases 141-144, 159-162, and 177-180; Table 1), requiring launches ~1 – 2.5 years before impact.

The number of resultant fragments varies for each diameter estimate in order to maintain an average fragment size of about 4 m, to remain consistent with findings in previous studies [6, 7].

4.5. Simulation Results

For our simulations of 2024 PDC25, we found that the ground effects of fragment airbursts resulting from mitigation via PI can be kept below their respective damage thresholds (Section 4.3) and are significantly lower than their unmitigated counterparts (Figure 6; Tables 1 and 2). The magnitude of the effects for any given case is dependent upon the physical parameters of the threat, namely diameter and density, and specific mitigation parameters, such as the number of resulting fragments and intercept time relative to ground impact. In general, increasing the number of fragments and/or intercept time will decrease the magnitude of the ground effects [5, 7].

To illustrate the magnitude of the ground effects, we plot the results of our simulations in the form of cumulative distribution functions (CDFs) of both optical energy flux and acoustic over-pressure in the ground plane. We use the CDF of a particular threat scenario to determine whether that scenario results in ground effects of acceptably low magnitude. In addition to the maximum value, a useful metric is the 1% value of the CDF for a particular threat scenario, which is the magnitude at which 1% of ground locations resolved in the simulation experience optical energy flux or acoustic over-pressure above that value. We refer to this value henceforth as the 1% CDF value.

While terminal mitigation of 2024 PDC25 would likely be unnecessary and undesirable, simulations suggest that PI could effectively remove the threat throughout a wide range of threat scenarios with very short warning times, and likely on timescales even shorter than shown here, depending on the object's physical characteristics.

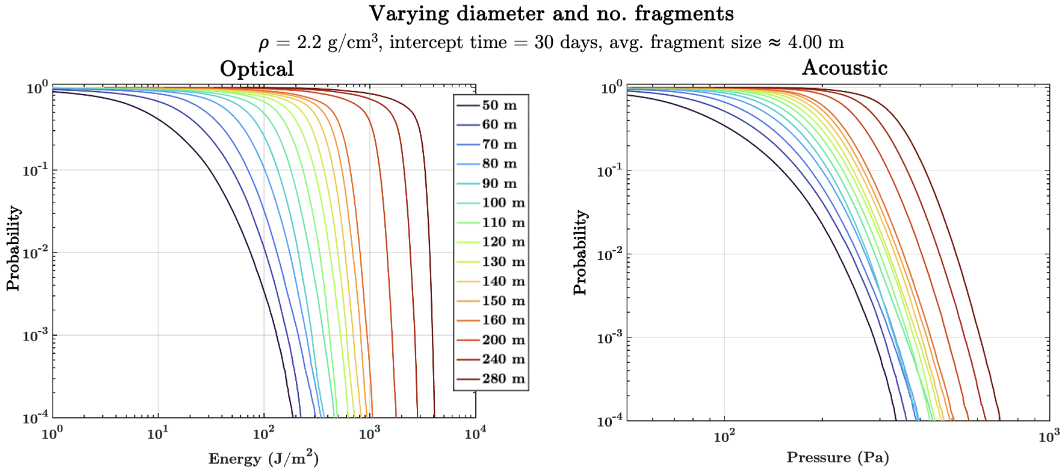

Figure 5: CDFs of the optical (left) and acoustic (right) ground effects of mitigated scenarios spanning the range of 2024 PDC25 diameter estimates (spherical equivalent). All scenarios assume an exo-atmospheric parent asteroid velocity (v_{exo}) of 13.725 km/s, average fragment disruption velocity (v_{dis}) of 1 m/s, entry angle of 69° relative to Earth's horizon, and average density of 2.2 g/cm^3. Mitigation scenarios assume an intercept time of 30 days prior to impact and vary in fragment number such that the average fragment size in each case is ~4.00 m.

4.5.1. Smaller Threat Range (50 - 130 m)

In Epoch 1–prior to data retrieval from the fast flyby reconnaissance mission–the size of 2024 PDC25 is highly uncertain at 48 – 278 m [28]. While this range is ultimately constrained to ~140 – 160 m in Epoch 2 [29], we simulate models for the lower end of the initial diameter estimate for comparison.

For unmitigated asteroids less than approximately 100 m in diameter and of weak porous to dense rock compositions (ρ = 1.0 – 4.0 g/cm^3), atmospheric entry would likely result in an airburst rather than ground impact. As a result, we simulate mitigated and unmitigated scenarios for asteroid models of 50 – 90 m in diameter (Figure 6; Tables 1 and 2).

Assuming an intercept time of 30 days, mitigation of weak porous asteroids (ρ = 1.0 – 2.0 g/cm^3) of 50 – 90 m yields 1% CDF values of approximately 0.03 – 0.19 kJ/m^2 for optical energy flux and 0.16 – 0.27 kPa for shock wave over-pressure. For stony to granitic asteroids (ρ = 2.2 – 2.8 g/cm^3), we find 1% CDF values of approximately 0.07 – 0.32 kJ/m^2 and 0.22 – 0.33 kPa. For dense rocky compositions (ρ = 3.0 – 4.0 g/cm^3), we find 1% CDF values of approximately 0.12 – 0.62 kJ/m^2 and 0.28 – 0.46 kPa. Previous studies estimate that even mitigation on drastically shorter timescales, such as an intercept one day before impact, would also be feasible [13, 7]; however, such extreme cases are not recommended. Longer intercepts are always preferred when possible.

For comparison, we estimate that an unfragmented spherical 50 m asteroid with an average density of 2.0 g/cm^3 would yield an average optical energy deposition of about 249 kJ/m^2 and average acoustic over-pressure of 3.4 kPa as experienced on the ground, with 1% CDF values of about 2400 kJ/m^2 and 13 kPa, respectively (Figure 6; Table 2). If the average density is increased to 2.8 g/cm^3, we find the average ground effects to be 465 kJ/m^2 and 4.2 kPa, with 1% CDF values of about 6000 kJ/m^2 and 23 kPa, respectively.

If the spherical diameter is increased to 90 m, we estimate that an unfragmented case with an average density of 2.0 g/cm^3 would yield average ground effects of 4173 kJ/m^2 and 14.6 kPa, with 1% CDF values of approximately 5.7E+4 kJ/m^2 and 120 kPa. For an average density of 2.8 g/cm^3, we find the average ground effects to be 3879 kJ/m^2 and 10.2 kPa, with 1% CDF values of about 5.6E+4 kJ/m^2 and 93 kPa, respectively (Figure 6; Table 2).

4.5.2. Likely Threat Range (140 - 160 m)

We highlight several threat cases within the 140 – 160 m diameter range (spherical estimates) as proxies for the "most likely" (68th %) size estimate for 2024 PDC25 [29].

Across the density range modeled (average density of 1.0 – 4.0 g/cm^3), we find that 30-day intercepts prior to impact with disruption into fragments of ~4.00 m (with fragment number varying with unbroken asteroid diameter) is sufficient to keep all ground effects below their damage thresholds (Figure 7; Table

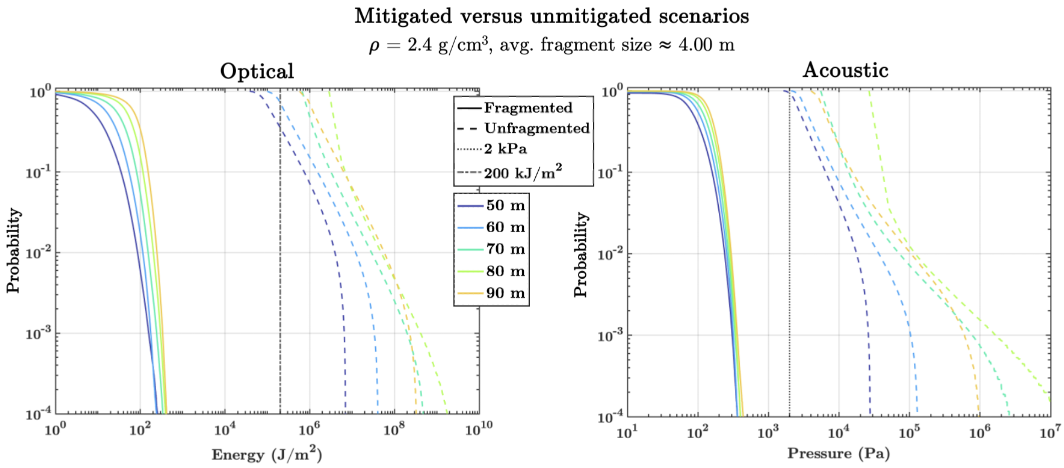

Figure 6: CDFs of the optical (left) and acoustic (right) ground effects of mitigated and unmitigated scenarios spanning the lower end of 2024 PDC25 diameter estimates. All scenarios assume an exo-atmospheric parent asteroid velocity (v_{exo}) of 13.725 km/s, entry angle of 69° relative to Earth's horizon, and average density of 2.4 g/cm^3; mitigated scenarios assume an intercept time of 30 days and an average fragment disruption velocity (v_{dis}) of 1 m/s. Mitigated scenarios vary in fragment number such that the average fragment size in each case is ~4.00 m. The dash-dotted black line (left) and dotted black line (right) mark the optical and acoustic damage thresholds of 200 kJ/m^2 and 2 kPa, respectively. Legend dictates diameter (spherical equivalent) and scenario type (fragmented versus unfragmented).

1). For weak porous asteroids (ρ = 1.0 – 2.0 g/cm^3) of 140 – 160 m, we find 1% CDF values of approximately 0.2 – 0.7 kJ/m^2 for optical energy flux and 0.2 – 0.3 kPa for shock wave over-pressure. For stony to granitic asteroids (ρ = 2.2 – 2.8 g/cm^3), we find 1% CDF values of approximately 0.5 – 1.2 kJ/m^2 and 0.3 – 0.4 kPa. For dense rock asteroids (ρ = 3.0 – 4.0 g/cm^3), we find 1% CDF values of approximately 1.0 – 2.2 kJ/m^2 and 0.4 – 0.6 kPa. It is likely that mitigation on even shorter timescales–which would be extreme–would also appear feasible, though such scenarios are not recommended.

Increasing the intercept time to 180 days decreases the magnitude of the ground effects. Applying this intercept time to the 140 – 160 m diameter range, we find 1% CDF values of approximately 2.6E-3 – 5.0E-3 kJ/m^2 and 0.1 – 0.2 kPa for ρ = 1.6 – 2.0 g/cm^3 and 7.6E-3 – 1.8E-2 kJ/m^2 and 0.1 – 0.2 kPa for for ρ = 2.4 – 2.8 g/cm^3 (Figure 7; Table 1).

4.5.3. Larger Threat Range (200 - 280 m)

We investigate terminal mitigation of asteroids on the higher end of the 2024 PDC25 diameter estimate for consistency with other simulated cases. Assuming a worst-case scenario of a 280 m diameter, dense-rock asteroid with an average density of 4.0 g/cm^3, we find that disruption of the body into 343,000 fragments with an intercept 30 days prior to impact would be sufficient to keep all ground effects well below their respective damage thresholds, as indicated by the 1% CDF values of 9.6 kJ/m^2 for optical energy flux and 0.8 kPa for shock wave over-pressure (Table 1).

Though, it should be noted that it would be highly unlikely for an object of this size to necessitate such a short-warning scenario. Realistically, if a large asteroid were to be on a collision course with Earth, it would likely be discovered many years prior to impact.

5. Discussion and Future Work

5.1. Summary of Results

Based on our simulation results, PI appears to be capable of mitigating threats like the hypothetical asteroid 2024 PDC25 for a variety of potential threat characteristics, achieving a reduction in ground effects when compared to analogous unmitigated threat cases (Tables 1 and 2; Figure 6). This is illustrated in Figure 8, which shows a comparison of the previously discussed simulation results for both the optical and acoustic ground effects. The 1% CDF values for optical energy flux (J/m^2) and acoustic over-pressure (Pa) are useful metrics for comparing the effectiveness of a given mitigation scenario

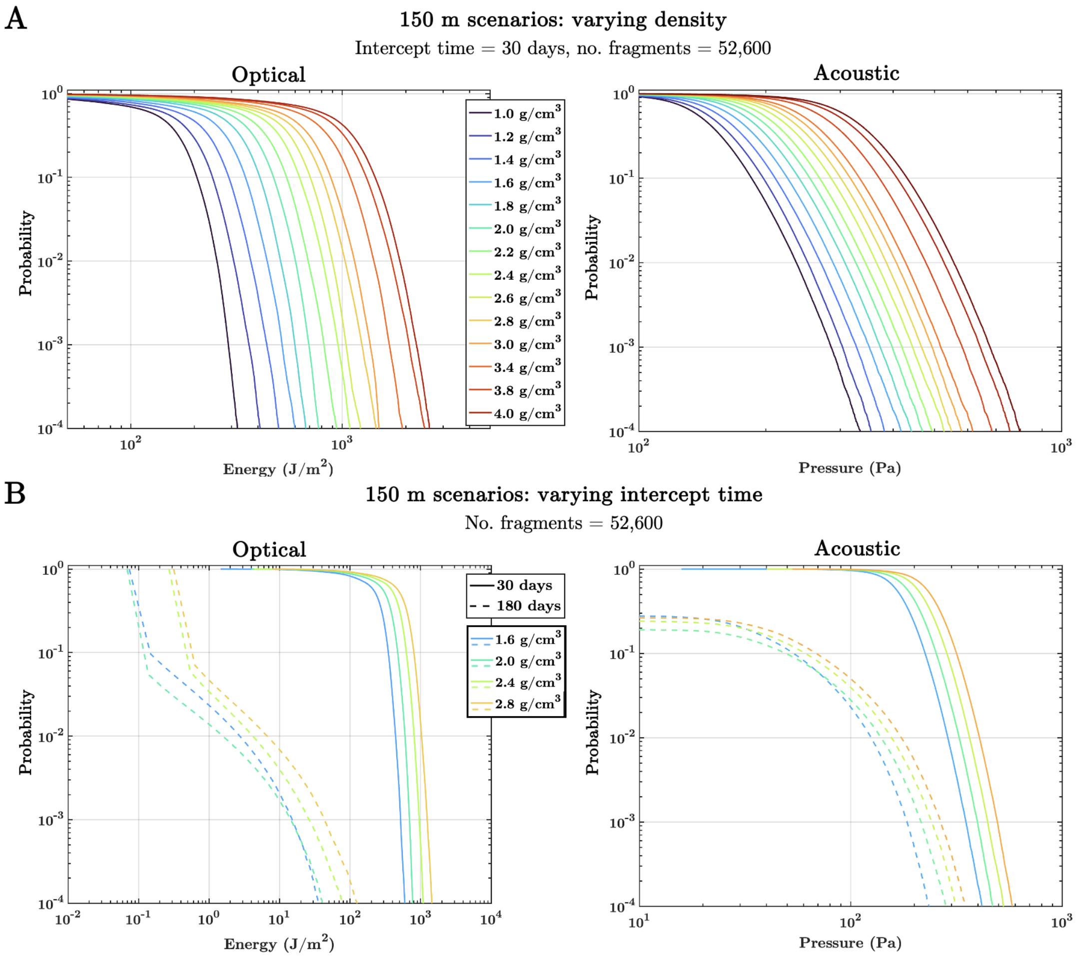

Figure 7: CDFs of the optical (left) and acoustic (right) ground effects of a 150 m spherical parent asteroid (proxy for the 2024 PDC25 likely diameter estimate) broken into 52,600 fragments (average fragment size of ∼4.00 m) with an intercept time of 30 days prior to impact. All scenarios assume an exo-atmospheric parent asteroid velocity (v_{exo}) of 13.725 km/s and entry angle of 69° relative to Earth's horizon. (A) Varying average density. Scenarios span the estimated density range of 2024 PDC25. Unbroken exo-atmospheric energies range from 39.8 – 111 Mt. (B) Varying density and intercept time. Legend dictates intercept time prior to impact and average density.

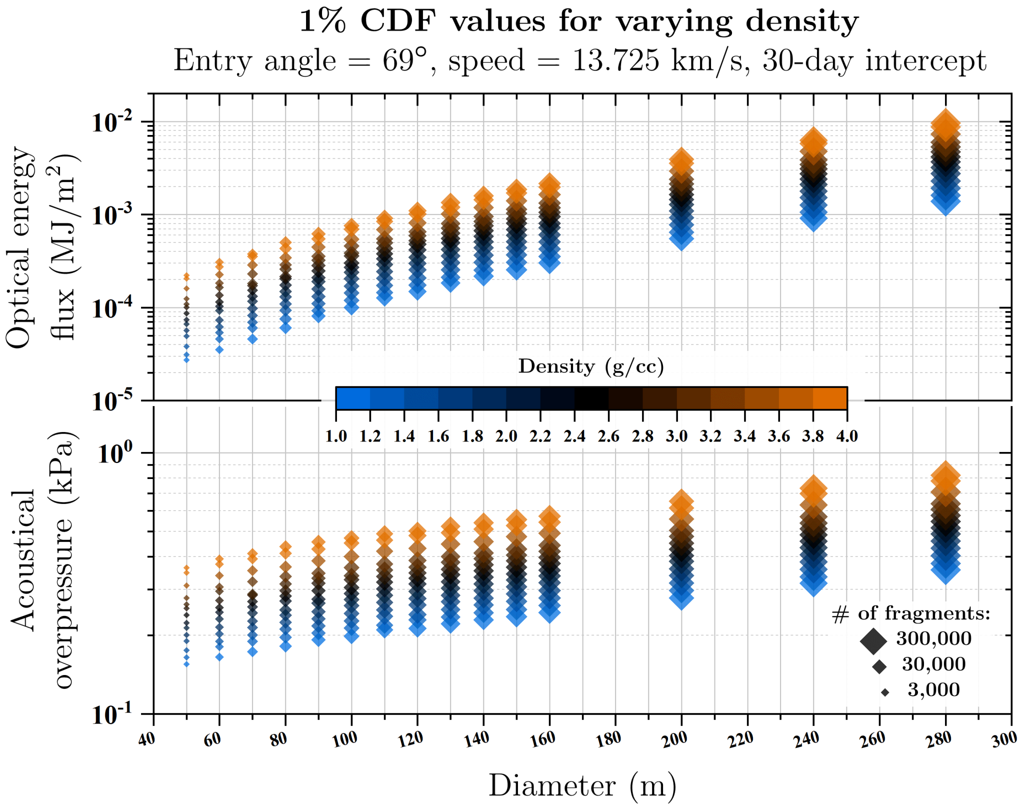

Figure 8: 1% CDF values for optical energy flux (upper) and acoustic over-pressure (lower) for mitigation scenarios of the hypothetical asteroid 2024 PDC25 with varying threat diameter (x-axis) and density (color scale). All scenarios assume an intercept 30 days prior to Earth impact. The number of fragments varies such that the average fragment size in each case is ~4.00 m. The marker size represents the number of fragments, as shown by the inset legend. Clear trends can be seen which show that reducing the target into a larger number of fragments is required to keep the 1% CDF values below the acceptable damage thresholds as the threat diameter and density are increased.

based on the magnitude of ground effects. The aggregated results, as shown in Figure 8, allows for some logical relationships to be resolved and illustrates the importance of considering mission-specific parameters, such as intercept time, impactor mass, and the number of fragments generated, when comparing mitigation scenarios.

5.2. Various Modes of Operation for 2024 PDC25

Intercept time–the length of time prior to Earth impact that the asteroid is intercepted–is a key parameter which could vastly alter the outcome of a mitigation scenario. In the hypothetical case of 2024 PDC25, the warning time is reasonably long, with discovery of the asteroid taking place nearly 17 years prior to impact. In a real scenario, any amount of warning time would be promptly taken advantage of, and it is likely that all appropriate parties would take action as quickly as possible.

Even in the early stages of detection of 2024 PDC25, when its physical and orbital characteristics are not yet well-defined, it is reasonable to assume that steps toward successful mitigation could be taken immediately. At the point of Epoch 1 on 1 August 2024, at which time the asteroid's orbital parameters and ranges for diameter and density are obtained (though still carrying some uncertainty), one could imagine investigating various conservative mitigation scenarios based on initial high-end estimates. It seems reasonable that the fast flyby reconnaissance mission and a potential mitigation mission could be designed concurrently, such that a planetary defense operation could be launched as soon as possible after the fast flyby data is retrieved.

It may then be possible that the four years between Epoch 1 and Epoch 2 could provide enough time for rapid development of PI, leading to operational status by the time the asteroid's characteristics are fully constrained. The authors acknowledge that PI has not yet reached an instrumented experimentation phase, though it is feasible that a focused and collaborative effort in a relatively short period could provide ample time to launch PI in an extended interdiction mode. Realization of PI as a mature and prepared planetary defense approach relies mainly on preexisting technologies (such as launch vehicles and foundations, as discussed in Section 3), providing the potential for rapid at-the-ready capability.

Upon obtaining the data collected by the fast flyby reconnaissance mission in April 2028, feasible parameters for the launch (such as launch vehicle(s) and mass(es), required C3, and date) and mitigation design (such as required ΔV for disruption, penetrator configuration, and desired number of fragments following disruption) of an instrumented PI mission could be calculated with precision and launched years ahead of the April 2041 impact date.

On the other hand, if one is to make an extremely conservative assumption that maturation of PI could not be enacted years ahead of time, a terminal mitigation effort would remain feasible. The ground effects simulations presented in Section 4 represent such cases, though should be interpreted as worst-case scenarios in which other options are unavailable, or perhaps as “backup” operations in the event an initial mission fails or results in unintended or unsuccessful disruption.

5.3. Limitations of the Model

The results of these ground effects simulations in tandem with the hypervelocity impact simulations presented in Section 3 and previous studies [5, 6, 7] suggest that PI may be an effective strategy for mitigating objects like 2024 PDC25, even in the highly unlikely event of a terminal mitigation scenario. However, we acknowledge that our simulation results presented here represent a limited range of potential threat scenarios, which do not fully encompass a high-fidelity investigation of mitigation via PI for all possible NEOs. Our analogues for 2024 PDC25 assume spherical asteroids within a limited size range (50 – 280 m diameter) and with an impact velocity of 13.725 km/s. While we vary threat parameters such as the average density (1.0 – 4.0 g/cm^3) and intercept time (30 days and 180 days), it is important to note that the model presented here spans a limited range of the potential physical and impact parameters for 2024 PDC25, or any other possible NEO. While our full suite of simulations (of which only a small fraction are presented within this paper) span asteroid sizes of 15 – 1000 m in diameter and explore a variety of strength models [5, 13, 6], more work is needed to expand the simulation regime to encompass a wider range of potential threat scenarios.

Additionally, while our simulations suggest that asteroid disassembly via PI could mitigate the threat estimates presented here, this method has not yet been put into practice outside of simulations. Further work is needed to establish physical experiments to probe the testable components of the method (e.g., penetrator design, payload delivery, launch vehicles, hypervelocity impacts on a comprehensive range of threat analogues to verify fragment distributions, etc.) beyond the simulation phase.

5.4. Preparation versus Proposition

For the purpose of this exercise, we discuss in the previous section a possible strategy towards in situ development of PI due to the asteroid's discovery taking place in 2024, as PI is not yet a fully tested or implemented planetary defense method. It would be preferable to prepare such technologies ahead of time rather than wait for a scenario in which it may become relevant. However, this hypothetical example provides motivation for progression of additional–or alternative–mitigation methods.

One could argue that a robust planetary defense system should be comprised of methods that are established and operational prior to the discovery of an incoming threat, rather than for development to be delayed until a threat is realized. It would be advantageous for any mitigation method to have undergone reliable and repeated design and test phases–as practiced by NASA's Double Asteroid Redirection Test (DART) mission for kinetic impact–before relying on it in a real-world situation.

We propose that a robust planetary defense system would not be limited to a single mitigation strategy but would instead be a highly redundant and layered structure, akin to national defense systems. We envision the future of PI as being synergistic with existing mitigation strategies, such as deflection, which may be logistically favorable in certain threat scenarios, particularly those with long warning times. Rather than to design an individual mission or method for a given situation, as in the hypothetical case for 2024 PDC25, it may be desirable to design a planetary defense system capable of mitigating a wide variety of threats across a vast range of scenarios. Reasonable exploration and implementation of multiple mitigation methods could establish a multi-use, at-the-ready system that could prove effective against many different types of threats.

Additionally, a structure capable of deploying multiple missions and/or various different mitigation methods could provide additional security. In the event of a real threat scenario where every second counts, utilization of tested and prearranged systems would decrease complexity and increase the likelihood for successful mitigation. The reliance on or combination of multiple dependable techniques could act as a safeguard to bolster our response to potential threats. As there is currently no planetary defense strategy in place capable of mitigating short-warning threats, we presently lack a foolproof system.

6. Conclusion

The simulations in this study suggest that the Pulverize It (PI) approach for planetary defense is a method worthy of consideration. Capable of operating on both short and extended timelines, PI could offer significant advantages over other mitigation strategies, such as a multi-modal capability, including the ability to mitigate potential threats when given very little forewarning, and lower launch mass requirements.

For the 9th Planetary Defense Conference hypothetical asteroid impact scenario, our simulations demonstrate that spherical asteroid analogues spanning the estimated diameter (50 – 280 m) and density (1.0 – 4.0 g/cm^3) ranges of the hypothetical asteroid 2024 PDC25 could be successfully disrupted, reducing a potential impact threat and the subsequent damages to manageable levels. With relatively minor mass requirements, existing launch vehicles, like the SpaceX Falcon 9, and similar technologies (either preexisting or within reach) could be used to mitigate a wide range of asteroid threats.

Our findings highlight that PI could turn a potentially regionally devastating impact into a successful removal of the threat. Even in extreme scenarios with unrealistically short timescales, we find that terminal mitigation with a 30-day intercept prior to impact could mitigate the estimated 63 – 105 megaton TNT equivalent energy release from 2024 PDC25 into a series of dispersed optical pulses and de-correlated shock waves that would result in minimal effects at ground level. Our simulations estimate that, in scenarios that are designed appropriately for a given threat, it is possible to keep the ground effects far below their established damage thresholds of 200 kJ/m^2 for optical energy and 2 kPa for acoustic overpressures. This points to the viability of considering PI as part of a comprehensive planetary defense strategy.

Table 1: Summary of mitigated (fragmented) threat scenarios and estimated ground effects for 2024 PDC25. All scenarios assume a spherical parent asteroid with an impact velocity of 13.725 km/s, entry angle of 69°, and average fragment disruption of 1 m/s. *D* indicates parent asteroid diameter; ρ indicates average parent asteroid density; intercept time is defined as the length of time prior to ground impact that the asteroid is intercepted. Average fragment size for each case is ∼4.00 m.

Case no.	D (m)	ρ (km/m^3)	No. frag.	Intercept time	Unbroken exoatm. energy (Mt)	1% opt. CDF value (J/m^2)	Weighted avg. opt. energy (J/m^2)	1% ac. CDF value (Pa)	Weighted avg. pressure (Pa)
1	50	1000	1950	30 day	1.47E+00	2.74E+01	4.85E+00	1.55E+02	6.43E+01
2	50	1200	1950	30 day	1.77E+00	3.11E+01	5.46E+00	1.65E+02	6.75E+01
3	50	1400	1950	30 day	2.06E+00	3.83E+01	6.67E+00	1.75E+02	7.04E+01
4	50	1600	1950	30 day	2.36E+00	4.94E+01	8.06E+00	1.90E+02	7.45E+01
5	50	1800	1950	30 day	2.65E+00	5.68E+01	9.47E+00	2.00E+02	7.92E+01
6	50	2000	1950	30 day	2.95E+00	6.68E+01	1.12E+01	2.13E+02	8.38E+01
7	50	2200	1950	30 day	3.24E+00	7.43E+01	1.25E+01	2.23E+02	8.58E+01
8	50	2400	1950	30 day	3.54E+00	8.65E+01	1.45E+01	2.39E+02	9.28E+01
9	50	2600	1950	30 day	3.83E+00	1.01E+02	1.63E+01	2.54E+02	9.62E+01
10	50	2800	1950	30 day	4.13E+00	1.09E+02	1.78E+01	2.63E+02	9.98E+01
11	50	3000	1950	30 day	4.42E+00	1.25E+02	2.00E+01	2.78E+02	1.04E+02
12	50	3400	1950	30 day	5.01E+00	1.60E+02	2.44E+01	3.10E+02	1.12E+02
13	50	3800	1950	30 day	5.60E+00	2.06E+02	3.03E+01	3.47E+02	1.24E+02
14	50	4000	1950	30 day	5.89E+00	2.23E+02	3.25E+01	3.63E+02	1.27E+02
15	60	1000	3375	30 day	2.55E+00	3.52E+01	8.33E+00	1.65E+02	7.74E+01
16	60	1200	3375	30 day	3.06E+00	4.59E+01	1.00E+01	1.81E+02	8.18E+01
17	60	1400	3375	30 day	3.56E+00	5.39E+01	1.17E+01	1.90E+02	8.56E+01
18	60	1600	3375	30 day	4.07E+00	6.22E+01	1.38E+01	2.02E+02	9.10E+01
19	60	1800	3375	30 day	4.58E+00	7.31E+01	1.63E+01	2.15E+02	9.60E+01
20	60	2000	3375	30 day	5.09E+00	9.28E+01	1.96E+01	2.31E+02	1.01E+02
21	60	2200	3375	30 day	5.60E+00	1.03E+02	2.22E+01	2.45E+02	1.06E+02
22	60	2400	3375	30 day	6.11E+00	1.15E+02	2.46E+01	2.56E+02	1.11E+02

Table 1 (continued).

Case no.	D (m)	ρ (km/m^3)	No. frag.	Intercept time	Unbroken exoatm. energy (Mt)	1% opt. CDF value (J/m^2)	Weighted avg. opt. energy (J/m^2)	1% ac. CDF value (Pa)	Weighted avg. pressure (Pa)
23	60	2600	3375	30 day	6.62E+00	1.36E+02	2.82E+01	2.72E+02	1.18E+02
24	60	2800	3375	30 day	7.13E+00	1.65E+02	3.22E+01	2.95E+02	1.22E+02
25	60	3000	3375	30 day	7.64E+00	1.83E+02	3.62E+01	3.06E+02	1.27E+02
26	60	3400	3375	30 day	8.66E+00	2.27E+02	4.35E+01	3.39E+02	1.39E+02
27	60	3800	3375	30 day	9.67E+00	2.74E+02	5.25E+01	3.75E+02	1.50E+02
28	60	4000	3375	30 day	1.02E+01	3.08E+02	5.68E+01	3.92E+02	1.56E+02
29	70	1000	5360	30 day	4.04E+00	4.62E+01	1.34E+01	1.73E+02	8.77E+01
30	70	1200	5360	30 day	4.85E+00	6.03E+01	1.53E+01	1.90E+02	9.15E+01
31	70	1400	5360	30 day	5.66E+00	6.97E+01	1.86E+01	2.01E+02	9.77E+01
32	70	1600	5360	30 day	6.47E+00	8.20E+01	2.23E+01	2.14E+02	1.03E+02
33	70	1800	5360	30 day	7.28E+00	9.84E+01	2.63E+01	2.27E+02	1.09E+02
34	70	2000	5360	30 day	8.09E+00	1.17E+02	3.05E+01	2.43E+02	1.16E+02
35	70	2200	5360	30 day	8.89E+00	1.32E+02	3.44E+01	2.57E+02	1.21E+02
36	70	2400	5360	30 day	9.70E+00	1.54E+02	3.88E+01	2.69E+02	1.26E+02
37	70	2600	5360	30 day	1.05E+01	1.72E+02	4.43E+01	2.85E+02	1.34E+02
38	70	2800	5360	30 day	1.13E+01	1.81E+02	4.43E+01	2.88E+02	1.33E+02
39	70	3000	5360	30 day	1.21E+01	2.30E+02	5.59E+01	3.21E+02	1.48E+02
40	70	3400	5360	30 day	1.37E+01	2.88E+02	6.74E+01	3.54E+02	1.60E+02
41	70	3800	5360	30 day	1.54E+01	3.54E+02	8.08E+01	3.93E+02	1.73E+02
42	70	4000	5360	30 day	1.62E+01	3.77E+02	8.75E+01	4.11E+02	1.81E+02
43	80	1000	8000	30 day	6.03E+00	6.05E+01	1.96E+01	1.82E+02	9.62E+01
44	80	1200	8000	30 day	7.24E+00	7.53E+01	2.31E+01	1.96E+02	1.02E+02
45	80	1400	8000	30 day	8.45E+00	9.39E+01	2.79E+01	2.11E+02	1.08E+02
46	80	1600	8000	30 day	9.66E+00	1.10E+02	3.29E+01	2.24E+02	1.14E+02
47	80	1800	8000	30 day	1.09E+01	1.31E+02	3.86E+01	2.39E+02	1.21E+02
48	80	2000	8000	30 day	1.21E+01	1.49E+02	4.46E+01	2.51E+02	1.27E+02
49	80	2200	8000	30 day	1.33E+01	1.75E+02	5.27E+01	2.71E+02	1.37E+02
50	80	2400	8000	30 day	1.45E+01	2.04E+02	5.96E+01	2.83E+02	1.43E+02
51	80	2600	8000	30 day	1.57E+01	2.16E+02	6.61E+01	2.96E+02	1.49E+02
52	80	2800	8000	30 day	1.69E+01	2.60E+02	7.34E+01	3.15E+02	1.55E+02
53	80	3000	8000	30 day	1.81E+01	2.89E+02	8.21E+01	3.36E+02	1.63E+02
54	80	3400	8000	30 day	2.05E+01	3.45E+02	9.90E+01	3.66E+02	1.79E+02
55	80	3800	8000	30 day	2.29E+01	4.33E+02	1.22E+02	4.12E+02	1.96E+02
56	80	4000	8000	30 day	2.41E+01	5.03E+02	1.34E+02	4.37E+02	2.05E+02
57	90	1000	11400	30 day	8.59E+00	8.09E+01	2.83E+01	1.92E+02	1.05E+02
58	90	1200	11400	30 day	1.03E+01	9.30E+01	3.31E+01	2.04E+02	1.11E+02
59	90	1400	11400	30 day	1.20E+01	1.10E+02	3.85E+01	2.17E+02	1.16E+02
60	90	1600	11400	30 day	1.37E+01	1.31E+02	4.73E+01	2.31E+02	1.24E+02
61	90	1800	11400	30 day	1.55E+01	1.58E+02	5.52E+01	2.46E+02	1.32E+02
62	90	2000	11400	30 day	1.72E+01	1.91E+02	6.52E+01	2.66E+02	1.41E+02
63	90	2200	11400	30 day	1.89E+01	2.11E+02	7.35E+01	2.75E+02	1.47E+02
64	90	2400	11400	30 day	2.06E+01	2.47E+02	8.31E+01	2.96E+02	1.55E+02
65	90	2600	11400	30 day	2.23E+01	2.85E+02	9.46E+01	3.16E+02	1.63E+02
66	90	2800	11400	30 day	2.41E+01	3.24E+02	1.07E+02	3.31E+02	1.72E+02
67	90	3000	11400	30 day	2.58E+01	3.58E+02	1.18E+02	3.45E+02	1.78E+02
68	90	3400	11400	30 day	2.92E+01	4.48E+02	1.44E+02	3.86E+02	1.96E+02
69	90	3800	11400	30 day	3.27E+01	5.50E+02	1.74E+02	4.28E+02	2.15E+02
70	90	4000	11400	30 day	3.44E+01	6.19E+02	1.89E+02	4.56E+02	2.26E+02
71	100	1000	15600	30 day	1.18E+01	1.00E+02	3.86E+01	1.99E+02	1.12E+02
72	100	1200	15600	30 day	1.41E+01	1.20E+02	4.52E+01	2.13E+02	1.19E+02
73	100	1400	15600	30 day	1.65E+01	1.44E+02	5.41E+01	2.27E+02	1.26E+02
74	100	1600	15600	30 day	1.89E+01	1.71E+02	6.41E+01	2.43E+02	1.34E+02
75	100	1800	15600	30 day	2.12E+01	2.04E+02	7.66E+01	2.60E+02	1.42E+02
76	100	2000	15600	30 day	2.36E+01	2.39E+02	8.72E+01	2.74E+02	1.49E+02
77	100	2200	15600	30 day	2.59E+01	2.70E+02	1.01E+02	2.89E+02	1.59E+02
78	100	2400	15600	30 day	2.83E+01	3.00E+02	1.14E+02	3.05E+02	1.66E+02
79	100	2600	15600	30 day	3.06E+01	3.59E+02	1.31E+02	3.26E+02	1.76E+02
80	100	2800	15600	30 day	3.30E+01	3.87E+02	1.45E+02	3.39E+02	1.85E+02
81	100	3000	15600	30 day	3.54E+01	4.58E+02	1.64E+02	3.64E+02	1.94E+02
82	100	3400	15600	30 day	4.01E+01	5.44E+02	1.97E+02	4.01E+02	2.13E+02
83	100	3800	15600	30 day	4.48E+01	6.93E+02	2.41E+02	4.51E+02	2.34E+02
84	100	4000	15600	30 day	4.71E+01	7.61E+02	2.56E+02	4.72E+02	2.43E+02
85	110	1000	20800	30 day	1.57E+01	1.27E+02	5.22E+01	2.10E+02	1.20E+02
86	110	1200	20800	30 day	1.88E+01	1.45E+02	6.01E+01	2.18E+02	1.26E+02
87	110	1400	20800	30 day	2.20E+01	1.74E+02	7.22E+01	2.36E+02	1.34E+02
88	110	1600	20800	30 day	2.51E+01	2.07E+02	8.61E+01	2.51E+02	1.42E+02
89	110	1800	20800	30 day	2.82E+01	2.44E+02	1.01E+02	2.68E+02	1.52E+02
90	110	2000	20800	30 day	3.14E+01	2.92E+02	1.17E+02	2.85E+02	1.59E+02
91	110	2200	20800	30 day	3.45E+01	3.35E+02	1.35E+02	3.01E+02	1.70E+02

Table 1 (continued).

Case no.	D (m)	ρ (km/m^3)	No. frag.	Intercept time	Unbroken exoatm. energy (Mt)	1% opt. CDF value (J/m^2)	Weighted avg. opt. energy (J/m^2)	1% ac. CDF value (Pa)	Weighted avg. pressure (Pa)
92	110	2400	20800	30 day	3.77E+01	3.78E+02	1.54E+02	3.19E+02	1.78E+02
93	110	2600	20800	30 day	4.08E+01	4.34E+02	1.72E+02	3.36E+02	1.87E+02
94	110	2800	20800	30 day	4.39E+01	4.97E+02	1.94E+02	3.55E+02	1.96E+02
95	110	3000	20800	30 day	4.71E+01	5.50E+02	2.15E+02	3.75E+02	2.06E+02
96	110	3400	20800	30 day	5.33E+01	6.92E+02	2.64E+02	4.20E+02	2.28E+02
97	110	3800	20800	30 day	5.96E+01	8.48E+02	3.18E+02	4.63E+02	2.50E+02
98	110	4000	20800	30 day	6.28E+01	9.12E+02	3.48E+02	4.89E+02	2.63E+02
99	120	1000	27000	30 day	2.04E+01	1.49E+02	6.54E+01	2.12E+02	1.25E+02
100	120	1200	27000	30 day	2.44E+01	1.75E+02	7.79E+01	2.29E+02	1.32E+02
101	120	1400	27000	30 day	2.85E+01	2.08E+02	9.17E+01	2.40E+02	1.40E+02
102	120	1600	27000	30 day	3.26E+01	2.55E+02	1.12E+02	2.61E+02	1.51E+02
103	120	1800	27000	30 day	3.67E+01	2.99E+02	1.31E+02	2.77E+02	1.59E+02
104	120	2000	27000	30 day	4.07E+01	3.47E+02	1.53E+02	2.94E+02	1.69E+02
105	120	2200	27000	30 day	4.48E+01	4.19E+02	1.75E+02	3.15E+02	1.79E+02
106	120	2400	27000	30 day	4.89E+01	4.81E+02	2.02E+02	3.31E+02	1.89E+02
107	120	2600	27000	30 day	5.30E+01	5.24E+02	2.24E+02	3.46E+02	1.98E+02
108	120	2800	27000	30 day	5.70E+01	5.95E+02	2.50E+02	3.65E+02	2.08E+02
109	120	3000	27000	30 day	6.11E+01	6.55E+02	2.78E+02	3.87E+02	2.18E+02
110	120	3400	27000	30 day	6.93E+01	8.13E+02	3.39E+02	4.30E+02	2.41E+02
111	120	3800	27000	30 day	7.74E+01	1.02E+03	4.16E+02	4.82E+02	2.67E+02
112	120	4000	27000	30 day	8.15E+01	1.10E+03	4.44E+02	5.02E+02	2.76E+02
113	130	1000	34400	30 day	2.59E+01	1.84E+02	8.56E+01	2.22E+02	1.32E+02
114	130	1200	34400	30 day	3.11E+01	2.12E+02	9.97E+01	2.35E+02	1.39E+02
115	130	1400	34400	30 day	3.63E+01	2.54E+02	1.18E+02	2.51E+02	1.48E+02
116	130	1600	34400	30 day	4.14E+01	3.04E+02	1.40E+02	2.69E+02	1.57E+02
117	130	1800	34400	30 day	4.66E+01	3.59E+02	1.66E+02	2.84E+02	1.68E+02
118	130	2000	34400	30 day	5.18E+01	4.20E+02	1.94E+02	3.03E+02	1.78E+02
119	130	2200	34400	30 day	5.70E+01	4.97E+02	2.23E+02	3.20E+02	1.87E+02
120	130	2400	34400	30 day	6.22E+01	5.53E+02	2.54E+02	3.41E+02	1.98E+02
121	130	2600	34400	30 day	6.73E+01	6.34E+02	2.84E+02	3.58E+02	2.08E+02
122	130	2800	34400	30 day	7.25E+01	7.18E+02	3.19E+02	3.81E+02	2.20E+02
123	130	3000	34400	30 day	7.77E+01	8.00E+02	3.57E+02	4.01E+02	2.31E+02
124	130	3400	34400	30 day	8.80E+01	1.02E+03	4.36E+02	4.47E+02	2.55E+02
125	130	3800	34400	30 day	9.84E+01	1.20E+03	5.21E+02	4.95E+02	2.80E+02
126	130	4000	34400	30 day	1.04E+02	1.35E+03	5.73E+02	5.23E+02	2.94E+02
127	140	1000	43000	30 day	3.23E+01	2.18E+02	1.07E+02	2.29E+02	1.38E+02
128	140	1200	43000	30 day	3.88E+01	2.52E+02	1.23E+02	2.44E+02	1.45E+02
129	140	1400	43000	30 day	4.53E+01	3.07E+02	1.49E+02	2.62E+02	1.55E+02
130	140	1600	43000	30 day	5.17E+01	3.66E+02	1.77E+02	2.77E+02	1.65E+02
131	140	1800	43000	30 day	5.82E+01	4.42E+02	2.09E+02	2.97E+02	1.75E+02
132	140	2000	43000	30 day	6.47E+01	5.13E+02	2.41E+02	3.14E+02	1.86E+02
133	140	2200	43000	30 day	7.12E+01	5.82E+02	2.78E+02	3.34E+02	1.96E+02
134	140	2400	43000	30 day	7.76E+01	6.74E+02	3.15E+02	3.53E+02	2.07E+02
135	140	2600	43000	30 day	8.41E+01	7.59E+02	3.56E+02	3.72E+02	2.18E+02
136	140	2800	43000	30 day	9.06E+01	8.45E+02	4.01E+02	3.93E+02	2.31E+02
137	140	3000	43000	30 day	9.70E+01	9.53E+02	4.44E+02	4.13E+02	2.41E+02
138	140	3400	43000	30 day	1.10E+02	1.19E+03	5.39E+02	4.57E+02	2.65E+02
139	140	3800	43000	30 day	1.23E+02	1.44E+03	6.49E+02	5.10E+02	2.93E+02
140	140	4000	43000	30 day	1.29E+02	1.60E+03	7.15E+02	5.39E+02	3.09E+02
141	140	1600	43000	180 days	5.17E+01	2.61E+00	1.13E-01	1.20E+02	1.43E+01
142	140	2000	43000	180 days	6.47E+01	7.01E-01	4.39E-02	1.15E+02	6.98E+00
143	140	2400	43000	180 days	7.76E+01	7.61E+00	3.51E-01	1.59E+02	2.07E+01
144	140	2800	43000	180 days	9.06E+01	8.85E+00	3.95E-01	1.74E+02	2.07E+01
145	150	1000	52600	30 day	3.98E+01	2.55E+02	1.31E+02	2.36E+02	1.43E+02
146	150	1200	52600	30 day	4.77E+01	3.07E+02	1.52E+02	2.51E+02	1.52E+02
147	150	1400	52600	30 day	5.57E+01	3.69E+02	1.81E+02	2.69E+02	1.62E+02
148	150	1600	52600	30 day	6.36E+01	4.41E+02	2.18E+02	2.88E+02	1.72E+02
149	150	1800	52600	30 day	7.16E+01	5.10E+02	2.57E+02	3.07E+02	1.84E+02
150	150	2000	52600	30 day	7.96E+01	6.00E+02	2.98E+02	3.26E+02	1.94E+02
151	150	2200	52600	30 day	8.75E+01	6.90E+02	3.42E+02	3.44E+02	2.05E+02
152	150	2400	52600	30 day	9.55E+01	8.09E+02	3.94E+02	3.65E+02	2.17E+02
153	150	2600	52600	30 day	1.03E+02	8.96E+02	4.40E+02	3.85E+02	2.29E+02
154	150	2800	52600	30 day	1.11E+02	1.03E+03	4.94E+02	4.06E+02	2.40E+02
155	150	3000	52600	30 day	1.19E+02	1.14E+03	5.46E+02	4.28E+02	2.52E+02
156	150	3400	52600	30 day	1.35E+02	1.41E+03	6.71E+02	4.78E+02	2.80E+02
157	150	3800	52600	30 day	1.51E+02	1.71E+03	7.98E+02	5.27E+02	3.06E+02
158	150	4000	52600	30 day	1.59E+02	1.87E+03	8.78E+02	5.56E+02	3.23E+02
159	150	1600	52600	180 days	6.36E+01	2.74E+00	1.19E-01	1.25E+02	1.43E+01
160	150	2000	52600	180 days	7.96E+01	1.59E+00	8.08E-02	1.39E+02	1.18E+01

Table 1 (continued).

Case no.	D (m)	ρ (km/m^3)	No. frag.	Intercept time	Unbroken exoatm. energy (Mt)	1% opt. CDF value (J/m^2)	Weighted avg. opt. energy (J/m^2)	1% ac. CDF value (Pa)	Weighted avg. pressure (Pa)
161	150	2400	52600	180 days	9.55E+01	4.06E+00	1.91E-01	1.56E+02	1.55E+01
162	150	2800	52600	180 days	1.11E+02	6.62E+00	3.12E-01	1.73E+02	1.83E+01
163	160	1000	64000	30 day	4.83E+01	3.03E+02	1.59E+02	2.45E+02	1.49E+02
164	160	1200	64000	30 day	5.79E+01	3.55E+02	1.85E+02	2.60E+02	1.58E+02
165	160	1400	64000	30 day	6.76E+01	4.26E+02	2.22E+02	2.78E+02	1.68E+02
166	160	1600	64000	30 day	7.72E+01	5.08E+02	2.61E+02	2.96E+02	1.79E+02
167	160	1800	64000	30 day	8.69E+01	6.07E+02	3.10E+02	3.18E+02	1.90E+02
168	160	2000	64000	30 day	9.66E+01	7.22E+02	3.63E+02	3.38E+02	2.02E+02
169	160	2200	64000	30 day	1.06E+02	8.07E+02	4.14E+02	3.55E+02	2.13E+02
170	160	2400	64000	30 day	1.16E+02	9.50E+02	4.75E+02	3.77E+02	2.26E+02
171	160	2600	64000	30 day	1.26E+02	1.06E+03	5.34E+02	3.97E+02	2.38E+02
172	160	2800	64000	30 day	1.35E+02	1.19E+03	5.97E+02	4.20E+02	2.50E+02
173	160	3000	64000	30 day	1.45E+02	1.33E+03	6.66E+02	4.42E+02	2.63E+02
174	160	3400	64000	30 day	1.64E+02	1.64E+03	8.16E+02	4.92E+02	2.91E+02
175	160	3800	64000	30 day	1.83E+02	1.98E+03	9.74E+02	5.42E+02	3.21E+02
176	160	4000	64000	30 day	1.93E+02	2.16E+03	1.06E+03	5.72E+02	3.36E+02
177	160	1600	64000	180 days	7.72E+01	1.06E+00	4.83E-02	1.24E+02	1.14E+01
178	160	2000	64000	180 days	9.66E+01	4.99E+00	2.23E-01	1.51E+02	2.21E+01
179	160	2400	64000	180 days	1.16E+02	1.31E+01	6.30E-01	1.74E+02	2.92E+01
180	160	2800	64000	180 days	1.35E+02	1.76E+01	8.40E-01	1.95E+02	3.26E+01
181	200	1000	125000	30 day	9.43E+01	5.53E+02	3.09E+02	2.78E+02	1.73E+02
182	200	1200	125000	30 day	1.13E+02	6.44E+02	3.61E+02	2.97E+02	1.83E+02
183	200	1400	125000	30 day	1.32E+02	7.74E+02	4.31E+02	3.17E+02	1.95E+02
184	200	1600	125000	30 day	1.51E+02	9.28E+02	5.18E+02	3.39E+02	2.08E+02
185	200	1800	125000	30 day	1.70E+02	1.10E+03	6.06E+02	3.60E+02	2.21E+02
186	200	2000	125000	30 day	1.89E+02	1.28E+03	7.09E+02	3.84E+02	2.35E+02
187	200	2200	125000	30 day	2.07E+02	1.46E+03	8.08E+02	4.04E+02	2.47E+02
188	200	2400	125000	30 day	2.26E+02	1.65E+03	9.18E+02	4.27E+02	2.60E+02
189	200	2600	125000	30 day	2.45E+02	1.87E+03	1.04E+03	4.51E+02	2.75E+02
190	200	2800	125000	30 day	2.64E+02	2.15E+03	1.17E+03	4.78E+02	2.91E+02
191	200	3000	125000	30 day	2.83E+02	2.39E+03	1.30E+03	5.05E+02	3.06E+02
192	200	3400	125000	30 day	3.21E+02	2.93E+03	1.58E+03	5.58E+02	3.37E+02
193	200	3800	125000	30 day	3.58E+02	3.56E+03	1.89E+03	6.15E+02	3.71E+02
194	200	4000	125000	30 day	3.77E+02	3.95E+03	2.08E+03	6.52E+02	3.91E+02
195	240	1000	216000	30 day	1.63E+02	9.16E+02	5.33E+02	3.17E+02	1.97E+02
196	240	1200	216000	30 day	1.96E+02	1.06E+03	6.21E+02	3.35E+02	2.09E+02
197	240	1400	216000	30 day	2.28E+02	1.27E+03	7.50E+02	3.58E+02	2.24E+02
198	240	1600	216000	30 day	2.61E+02	1.53E+03	8.91E+02	3.83E+02	2.38E+02
199	240	1800	216000	30 day	2.93E+02	1.79E+03	1.05E+03	4.07E+02	2.53E+02
200	240	2000	216000	30 day	3.26E+02	2.11E+03	1.22E+03	4.33E+02	2.69E+02
201	240	2200	216000	30 day	3.58E+02	2.41E+03	1.40E+03	4.58E+02	2.84E+02
202	240	2400	216000	30 day	3.91E+02	2.75E+03	1.60E+03	4.85E+02	3.00E+02
203	240	2600	216000	30 day	4.24E+02	3.12E+03	1.80E+03	5.12E+02	3.16E+02
204	240	2800	216000	30 day	4.56E+02	3.46E+03	2.00E+03	5.39E+02	3.32E+02
205	240	3000	216000	30 day	4.89E+02	3.87E+03	2.24E+03	5.69E+02	3.50E+02
206	240	3400	216000	30 day	5.54E+02	4.81E+03	2.74E+03	6.30E+02	3.86E+02
207	240	3800	216000	30 day	6.19E+02	5.82E+03	3.28E+03	6.98E+02	4.26E+02
208	240	4000	216000	30 day	6.52E+02	6.30E+03	3.58E+03	7.31E+02	4.47E+02
209	280	1000	343000	30 day	2.59E+02	1.39E+03	8.49E+02	3.56E+02	2.25E+02
210	280	1200	343000	30 day	3.10E+02	1.62E+03	9.89E+02	3.77E+02	2.38E+02
211	280	1400	343000	30 day	3.62E+02	1.93E+03	1.18E+03	4.03E+02	2.54E+02
212	280	1600	343000	30 day	4.14E+02	2.31E+03	1.41E+03	4.31E+02	2.71E+02
213	280	1800	343000	30 day	4.66E+02	2.76E+03	1.66E+03	4.59E+02	2.88E+02
214	280	2000	343000	30 day	5.17E+02	3.20E+03	1.95E+03	4.89E+02	3.06E+02
215	280	2200	343000	30 day	5.69E+02	3.68E+03	2.22E+03	5.16E+02	3.23E+02
216	280	2400	343000	30 day	6.21E+02	4.17E+03	2.53E+03	5.45E+02	3.41E+02
217	280	2600	343000	30 day	6.73E+02	4.74E+03	2.86E+03	5.75E+02	3.60E+02
218	280	2800	343000	30 day	7.24E+02	5.33E+03	3.20E+03	6.07E+02	3.79E+02
219	280	3000	343000	30 day	7.76E+02	5.97E+03	3.56E+03	6.39E+02	3.98E+02
220	280	3400	343000	30 day	8.80E+02	7.31E+03	4.35E+03	7.08E+02	4.39E+02
221	280	3800	343000	30 day	9.83E+02	8.77E+03	5.22E+03	7.81E+02	4.84E+02
222	280	4000	343000	30 day	1.03E+03	9.65E+03	5.68E+03	8.21E+02	5.07E+02

Table 2: Summary of unmitigated (unfragmented) threat scenarios and estimated ground effects for 2024 PDC25. All scenarios assume a spherical parent asteroid with an impact velocity of 13.725 km/s and entry angle of 69°. *D* indicates parent asteroid diameter; ρ indicates average parent asteroid density. Note that the maximum optical energy and maximum pressure values are experienced at the lowest probability level of the simulation, which may vary between cases.

Case no.	D (m)	ρ (kg/m^3)	Unbroken exoatm. energy (Mt)	1% opt. CDF value (J/m^2)	Weighted avg. opt. energy (J/m^2)	Max. opt. energy (J/m^2)	1% ac. CDF value (Pa)	Weighted avg. pressure (Pa)	Max. pressure (Pa)
223	50	1600	2.36E+00	1.37E+06	1.70E+05	1.84E+06	1.00E+04	3.05E+03	1.21E+04
224	50	2000	2.95E+00	2.42E+06	2.49E+05	3.65E+06	1.34E+04	3.44E+03	1.80E+04
225	50	2400	3.54E+00	3.95E+06	3.47E+05	7.03E+06	1.77E+04	3.83E+03	2.80E+04
226	50	2800	4.13E+00	6.04E+06	4.65E+05	1.36E+07	2.32E+04	4.24E+03	4.76E+04
227	60	1600	4.07E+00	4.13E+06	3.87E+05	6.83E+06	1.78E+04	4.01E+03	2.63E+04
228	60	2000	5.09E+00	7.50E+06	5.84E+05	1.64E+07	2.59E+04	4.62E+03	5.31E+04
229	60	2400	6.11E+00	1.22E+07	8.42E+05	4.14E+07	3.67E+04	5.34E+03	1.34E+05
230	60	2800	7.13E+00	1.79E+07	1.20E+06	1.23E+08	4.93E+04	6.38E+03	4.95E+05
231	70	1600	6.47E+00	1.09E+07	8.07E+05	2.70E+07	3.27E+04	5.24E+03	8.05E+04
232	70	2000	8.09E+00	1.91E+07	1.28E+06	9.59E+07	5.04E+04	6.48E+03	3.37E+05
233	70	2400	9.70E+00	2.87E+07	2.05E+06	5.62E+08	7.27E+04	9.16E+03	3.20E+06
234	70	2800	1.13E+01	7.84E+08	5.29E+06	3.92E+11	8.63E+07	1.49E+05	4.32E+10
235	80	1600	9.66E+00	2.42E+07	1.62E+06	1.39E+08	5.95E+04	7.25E+03	4.91E+05
236	80	2000	1.21E+01	3.94E+07	3.05E+06	2.06E+09	1.13E+05	1.35E+04	1.84E+07
237	80	2400	1.45E+01	4.87E+07	3.78E+06	2.70E+09	1.23E+05	1.56E+04	2.40E+07
238	80	2800	1.69E+01	4.94E+07	3.32E+06	4.25E+08	9.65E+04	1.06E+04	1.54E+06
239	90	1600	1.37E+01	4.63E+07	3.53E+06	2.43E+09	1.10E+05	1.49E+04	2.14E+07
240	90	2000	1.72E+01	5.66E+07	4.17E+06	1.66E+09	1.19E+05	1.46E+04	1.06E+07
241	90	2400	2.06E+01	5.76E+07	3.84E+06	3.41E+08	1.04E+05	1.09E+04	1.02E+06
242	90	2800	2.41E+01	5.56E+07	3.88E+06	1.76E+08	9.32E+04	1.02E+04	3.87E+05

Acknowledgments

We gratefully acknowledge funding from NASA Innovative Advanced Concepts (NIAC) Phase I grant 80NSSC22K0764, NIAC Phase II grant 80NSSC23K0966, and NASA California Space Grant NNX10AT93H, as well as from the Emmett and Gladys W. Fund. We gratefully acknowledge support from the NASA Ames High End Computing Capability (HECC) group and Lawrence Livermore National Laboratory (LLNL) for the use of their ALE3D simulation tools used for modeling the hypervelocity penetrator impacts and for funding from NVIDIA for an Academic Hardware Grant for a high-end GPU greatly speeding up ground effect simulations. We would like to thank our large team of researchers, collaborators, and undergraduates for their tireless work and enthusiasm to defend the planet.

References

[1] L. Wheeler, J. Dotson, A. Coates, M. Aftosmis, E. Stern, D. L. Mathias, Impact Risk Assessment: PDC25 Hypothetical Asteroid Impact Exercise, Epoch 1 – Initial Threat Discovery & SMPAG Notification, 2024.

[2] L. Wheeler, J. Dotson, A. Coates, M. Aftosmis, E. Stern, D. L. Mathias, Impact Risk Assessment: PDC25 Hypothetical Asteroid Impact Exercise, Epoch 2 – Flyby Reconnaissance Mission Data, 2024.

[3] N. S. E. Team, Near-Earth Asteroids as of April 2025, 2025. Section: Planetary Defense.

[4] A. W. Harris, P. W. Chodas, The population of near-earth asteroids revisited and updated, Icarus 365 (2021) 114452.

[5] P. Lubin, A. N. Cohen, Asteroid interception and disruption for terminal planetary defense, Advances in Space Research 71 (2023) 1827–1839.

[6] A. N. Cohen, P. Lubin, D. Robertson, M. Boslough, S. Egan, A. M. Stickle, E. A. Silber, P. Meinhold, B. Bailey, D. Patel, Asteroid disruption and deflection simulations for multi-modal planetary defense, Acta Astronautica 225 (2024) 960–967.

[7] B. Bailey, A. N. Cohen, S. Egan, P. Lubin, R. Xu, M. Boslough, D. Robertson, E. A. Silber, I. Sagert, O. Korobkin, G. Sjoden, Evaluating Short-warning Mitigation via Intentional Robust Disruption of a Hypothetical Impact of Asteroid 2023 NT1, The Astrophysical Journal 981 (2025) 181. Publisher: The American Astronomical Society.

[8] A. S. Rivkin, N. L. Chabot, A. M. Stickle, C. A. Thomas, D. C. Richardson, O. Barnouin, E. G. Fahnestock, C. M. Ernst, A. F. Cheng, S. Chesley, S. Naidu, T. S. Statler, B. Barbee, H. Agrusa, N. Moskovitz, R. T. Daly, P. Pravec, P. Scheirich, E. Dotto, V. D. Corte, P. Michel, M. Küppers, J. Atchison, M. Hirabayashi, The Double Asteroid Redirection Test (DART): Planetary Defense Investigations and Requirements, The Planetary Science Journal 2 (2021) 173. Publisher: IOP Publishing.

[9] D. S. P. Dearborn, M. Bruck Syal, B. W. Barbee, G. Gisler, K. Greenaugh, K. M. Howley, R. Leung, J. Lyzhoft, P. L. Miller, J. A. Nuth, C. S. Plesko, B. D. Seery, J. V. Wasem, R. P. Weaver, M. Zebenay, Options and uncertainties in planetary defense: Impulse-dependent response and the physical properties of asteroids, Acta Astronautica 166 (2020) 290–305.

[10] D. C. Hyland, H. A. Altwaijry, S. Ge, R. Margulieux, J. Doyle, J. Sandberg, B. Young, X. Bai, J. Lopez, N. Satak, A permanently-acting NEA damage mitigation technique via the Yarkovsky effect, Cosmic Research 48 (2010) 430–436.

[11] D. D. Mazanek, D. M. Reeves, J. B. Hopkins, D. W. Wade, M. Tantardini, H. Shen, Enhanced Gravity Tractor Technique for Planetary Defense, Frascati, Roma. NTRS Author Affiliations: NASA Langley Research Center, Lockheed Martin Space Systems Co., , Analytical Mechanics Associates, Inc. NTRS Report/Patent Number: IAA-PDC-15-04-11 NTRS Document ID: 20150010968 NTRS Research Center: Langley Research Center (LaRC).

[12] R. Walker, D. Izzo, C. de Negueruela, L. Summerer, M. Ayre, M. Vasile, Concepts for Near-Earth Asteroid Deflection using Spacecraft with Advanced Nuclear and Solar Electric Propulsion Systems, Journal of the British Interplanetary Society 58 (2005) 268–278. ADS Bibcode: 2005JBIS...58..268W.

[13] B. Bailey, A. N. Cohen, P. Lubin, D. Robertson, M. Boslough, S. Egan, E. A. Silber, D. Patel, Optical and acoustic ground effects simulations from terminal defense asteroid disruption via the PI method, Acta Astronautica 221 (2024) 230–239.

[14] D. A. Kring, M. Boslough, Chelyabinsk: Portrait of an asteroid airburst, Physics Today 67 (2014) 32–37.

[15] D. K. Robertson, D. L. Mathias, Effect of yield curves and porous crush on hydrocode simulations of asteroid airburst, Journal of Geophysical Research: Planets 122 (2017) 599–613. _eprint: https://onlinelibrary.wiley.com/doi/pdf/10.1002/2016JE005194.

[16] C. Noble, A. Anderson, N. Barton, J. Bramwell, A. Capps, M. Chang, J. Chou, D. Dawson, E. Diana, T. Dunn, D. Faux, A. Fisher, P. Greene, I. Heinz, Y. Kanarska, S. Khairallah, B. Liu, J. Margraf, A. Nichols, J. White, ALE3D: An Arbitrary Lagrangian-Eulerian Multi-Physics Code, Technical Report LLNL-TR-732040, Lawrence Livermore National Lab, 2017.

[17] P. Sánchez, D. J. Scheeres, The strength of regolith and rubble pile asteroids, Meteoritics & Planetary Science 49 (2014) 788–811. _eprint: https://onlinelibrary.wiley.com/doi/pdf/10.1111/maps.12293.

[18] P. Pravec, A. W. Harris, Fast and Slow Rotation of Asteroids, Icarus 148 (2000) 12–20.

[19] K. R. Housen, W. J. Sweet, K. A. Holsapple, Impacts into porous asteroids, Icarus 300 (2018) 72–96.

[20] K. R. Housen, K. A. Holsapple, Deflecting Asteroids by Impacts: What is Beta?, p. 2539. ADS Bibcode: 2012LPI....43.2539H.

[21] K. A. Holsapple, K. R. Housen, Momentum transfer in asteroid impacts. I. Theory and scaling, Icarus 221 (2012) 875–887.

[22] K. A. Holsapple, R. M. Schmidt, Point source solutions and coupling parameters in cratering mechanics, Journal of Geophysical Research: Solid Earth 92 (1987) 6350–6376. _eprint: https://onlinelibrary.wiley.com/doi/pdf/10.1029/JB092iB07p06350.

[23] A. F. Cheng, H. F. Agrusa, B. W. Barbee, A. J. Meyer, T. L. Farnham, S. D. Raducan, D. C. Richardson, E. Dotto, A. Zinzi, V. Della Corte, T. S. Statler, S. Chesley, S. P. Naidu, M. Hirabayashi, J.-Y. Li, S. Eggl, O. S. Barnouin, N. L. Chabot, S. Chocron, G. S. Collins, R. T. Daly, T. M. Davison, M. E. DeCoster, C. M. Ernst, F. Ferrari, D. M. Graninger, S. A. Jacobson, M. Jutzi, K. M. Kumamoto, R. Luther, J. R. Lyzhoft, P. Michel, N. Murdoch, R. Nakano, E. Palmer, A. S. Rivkin, D. J. Scheeres, A. M. Stickle, J. M. Sunshine, J. M. Trigo-Rodriguez, J.-B. Vincent, J. D. Walker, K. Wünnemann, Y. Zhang, M. Amoroso, I. Bertini, J. R. Brucato, A. Capannolo, G. Cremonese, M. Dall'Ora, P. J. D. Deshapriya, I. Gai, P. H. Hasselmann, S. Ieva, G. Impresario, S. L. Ivanovski, M. Lavagna, A. Lucchetti, E. M. Epifani, D. Modenini, M. Pajola, P. Palumbo, D. Perna, S. Pirrotta, G. Poggiali, A. Rossi, P. Tortora, M. Zannoni, G. Zanotti, Momentum transfer from the DART mission kinetic impact on asteroid Dimorphos, Nature 616 (2023) 457–460. Publisher: Nature Publishing Group.

[24] P. Brown, R. E. Spalding, D. O. ReVelle, E. Tagliaferri, S. P. Worden, The flux of small near-Earth objects colliding with the Earth, Nature 420 (2002) 294–296. Number: 6913 Publisher: Nature Publishing Group.

[25] S. Glasstone, P. J. Dolan, The Effects of Nuclear Weapons. Third edition, Technical Report TID-28061, Department of Defense, Washington, D.C. (USA), 1977.

[26] M. Boslough, P. Brown, A. Harris, Updated population and risk assessment for airbursts from near-earth objects (NEOs), in: 2015 IEEE Aerospace Conference, pp. 1–12. ISSN: 1095-323X.

[27] S. Martin, Diffusion-controlled ignition of cellulosic materials by intense radiant energy, Symposium (International) on Combustion 10 (1965) 877–896.

[28] L. Wheeler, J. Dotson, A. Coates, M. Aftosmis, E. Stern, D. L. Mathias, Planetary Defense Conference Exercise - 2025, Epoch 1, 2024.

[29] L. Wheeler, J. Dotson, A. Coates, M. Aftosmis, E. Stern, D. L. Mathias, Planetary Defense Conference Exercise - 2025, Epoch 2, 2024.